Journal of Colloid and Interface Science 691 (2025) 137400

Contents lists available at ScienceDirect

Journal of Colloid And Interface Science

journal homepage: www.elsevier.com/locate/jcis

Controllable synthesis of In-Plane Mo/Mo_2C heterojunction nanosheets for enhanced hydrogen evolution reaction

Yulei Ren [a,b,1], Rui Huo [e,1], Xiuli Li [a], Hao Song [a,*], Xuming Zhang [a], Biao Gao [a], Paul K. Chu [c], Kaifu Huo [b,d,*]

[a] State Key Laboratory of Advanced Refractories, Institute of Advanced Materials and Nanotechnology, Wuhan University of Science and Technology, Wuhan 430081, China
[b] Wuhan National Laboratory for Optoelectronics (WNLO), School of Optical and Electronic Information, Huazhong University of Science and Technology, Wuhan 430074, China
[c] Department of Physics, Department of Materials Science and Engineering, and Department of Biomedical Engineering, City University of Hong Kong, Tat Chee Avenue, Kowloon, Hong Kong, China
[d] Research Institute of Huazhong University of Science and Technology in Shenzhen, Shenzhen 518063, China
[e] School of Materials Science and Engineering, Central South University, Changsha 410083, China

GRAPHICAL ABSTRACT

2D in-plane Mo/Mo_2C heterojunction nanosheets electrocatalyst is manufactured from bulk MoS_2 via a molten salt-assisted approach. The electron transfer from Mo to Mo_2C and fill Mo_2C antibonding orbitals, which weakens Mo-H bonding, enhances H_2O adsorption and dissociation, optimizes H adsorption/desorption of in-plane Mo/Mo_2C heterojunction nanosheets, thereby promoting the HER kinetics.

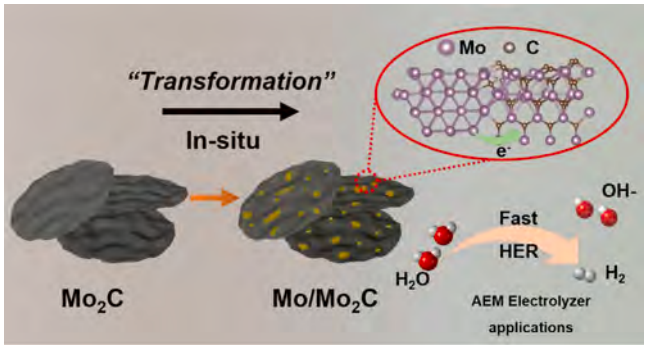

ARTICLE INFO

Keywords:
Molybdenum carbide
2D nanosheets
In-plane heterostructure
Mo-H bonding
Hydrogen evolution reaction

ABSTRACT

Two-dimensional (2D) molybdenum carbide (Mo_2C) is a potential electrocatalyst for the hydrogen evolution reaction (HER) due to its Pt-like electronic structure, high electrical conductivity, and abundant active sites. However, its practical application as an HER catalyst is hindered by the sluggish kinetics due to the strong hydrogen absorption. Herein, 2D in-plane Mo/Mo_2C heterojunction nanosheets are synthesized from bulk molybdenum disulfide (MoS_2) via a molten salt-assisted technique. The ultraviolet photoelectron spectra combined with density-functional theory (DFT) simulations elucidates that electrons are transferred from Mo to Mo_2C and

* Corresponding authors.
E-mail addresses: songhao201809@wust.edu.cn (H. Song), kfhuo@hust.edu.cn (K. Huo).
[1] Yulei Ren, and Rui Huo contributed equally to this work.

https://doi.org/10.1016/j.jcis.2025.137400
Received 10 February 2025; Received in revised form 19 March 2025; Accepted 19 March 2025
Available online 20 March 2025

fill Mo_2C antibonding orbitals, which weakens Mo-H bonding, enhances H_2O adsorption and dissociation, optimizes H adsorption/desorption of in-plane Mo/Mo_2C heterojunction nanosheets, thus promoting the HER kinetics. The Mo/Mo_2C heterojunction nanosheets electrocatalyst demonstrates exceptional HER performance with minimal overpotentials (90 mV in alkaline vs. 96 mV in acidic media at 10 mA cm^{-2}) and favorable Tafel slopes (54.9 vs. 64.2 mV dec^{-1}). Notably, it achieves a 280 mV overpotential at 500 mA cm^{-2} under alkaline conditions, surpassing that of the commercial Pt/C electrode. The stability is excellent as confirmed by an increase of potential of only about 10 mV after operation for 100 h at 300 mA cm^{-2}. The results reveal a simple and effective strategy to boost the catalytic HER activity boding well for high-efficiency commercial water splitting.

1. Introduction

Hydrogen (H_2) produced by water splitting is a highly promising, efficient, eco-friendly, economical, and sustainable energy source.[1–5] In water electrolysis, the hydrogen evolution reactions (HER) efficiency depends on electrocatalyst performance. Therefore, the development of highly efficient and sustainable electrocatalysts is crucial for optimizing reaction kinetics.[6–8] While Pt has the highest intrinsic HER catalytic activity, its scarcity-driven cost presents substantial barriers to scalable implementation.[9,10] In this respect, developing earth-abundant electrocatalysts with noble metal-mimetic HER activity is crucial to the development of clean hydrogen.[11–13] Among the various non–precious metal-based electrocatalysts, two-dimensional (2D) molybdenum carbide (Mo_2C) has emerged as a potential alternative to Pt because of its Pt-mimetic electronic configuration, superior charge mobility, large surface area, and ample active sites.[14–16] Nevertheless, the strong Mo-H bond in Mo_2C gives rise to a low occupancy state of Mo 4*d* antibonding orbitals, specifically impeding hydrogen desorption in the Tafel or Heyrovsky step for HER.[17,18].

2D Mo_2C-based hetero-structured electrocatalysts can be designed by modulating the electronic configuration to weaken the Mo-H bond. Liu et al. have reported a Ni/Mo_2C hetero-sheet array electrocatalyst with enhanced HER activity in the alkaline electrolyte because a larger electron density of Mo_2C is observed near the Fermi level as a result of the interfacial interaction of Ni and Mo_2C.[19] Wang et al. have reported that MoS_2 nanosheets grown on 2D Mo_2C show enhanced intrinsic HER activity, achieving an overpotential reduction to 207 mV from 700 mV of pristine 2D Mo_2C at 10 mA cm^{-2}.[20] Nevertheless, the fabrication of 2D Mo_2C-based hetero-structured nanosheets often involves intricate processes and the composites deposited on Mo_2C nanosheets compromise active sites, thereby limiting the HER activity. In this context, 2D in-plane Mo_2C-based heterojunctions which can simultaneously boost the number of active sites and optimize hydrogen absorption/desorption, have large potential in HER.

Herein, we report in-plane Mo/Mo_2C heterojunction nanosheets with a precisely regulated interface and abundant electrochemical active sites as high-efficiency electrocatalysts for HER with pH-universal. The 2D Mo/Mo_2C hetero-structured are synthesized from the commercial MoS_2 by Na_2CO_3-assisted thermal carbonization, followed by annealing under Ar/H_2 to partially remove interstitial carbon atoms from the Mo_2C nanosheets. The composition of Mo/Mo_2C can be adjusted and controlled by altering the annealing duration in Ar/H_2. The as-synthesized 2D Mo/Mo_2C nanosheet has a thickness of about 8.2 nm and abundant electroactive sites for HER. The ultraviolet photoelectron spectra and density-functional theory (DFT) simulations elucidate that electrons migrate from Mo to Mo_2C at the Mo/Mo_2C heterointerface to enhance the Mo 4*d* antibonding-orbital occupancy state of Mo_2C, consequently improving H_2O adsorption/dissociation, optimizing H adsorption/desorption, and improving the HER efficiency (Fig. 1a). The 2D Mo/Mo_2C heterojunction electrocatalyst delivers superior HER performances across wide pH conditions, achieving remarkably low overpotentials of 90 mV (alkaline) and 96 mV (acidic) at 10 mA cm^{-2} with corresponding Tafel slopes of 54.9 and 64.2 mV dec^{-1}. Notably, this catalyst exhibits outstanding high-current performance with a 280 mV overpotential at 500 mA cm^{-2}, outperforming commercial Pt/C (335 mV) and those of Mo_2C-based electrocatalysts reported recently.[15,16] The 2D Mo/Mo_2C hetero-structured electrocatalyst also shows excellent durability with unnoticeable decay at 300 mA cm^{-2} for 100 h. To demonstrate the commercial viability, an anion exchange membrane water electrolyzer composed of the Mo/Mo_2C cathode and NiFe-LDH anode achieves exceptional performance, requiring only 2.23 V to sustain 1,000 mA cm^{-2} current density. The results reveal a straight

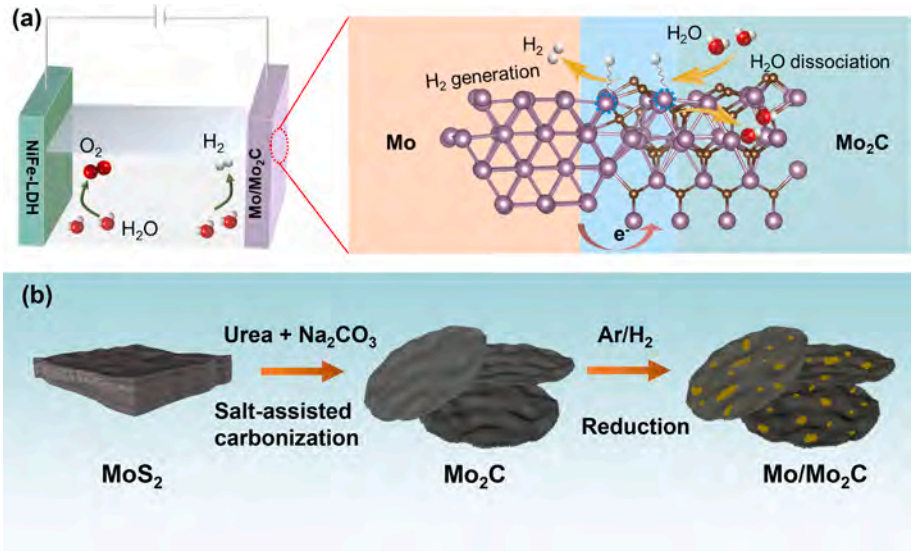

Fig. 1. (a) Schematic diagram of the Mo/Mo_2C||NiFe-LDH overall water splitting device. Electron transfer from Mo to Mo_2C at the Mo/Mo_2C heterointerface enhances H_2O adsorption and dissociation and promotes H desorption and HER kinetics; (b) Schematic illustration of the synthetic process of the 2D in-plane Mo/Mo_2C heterojunction from bulk MoS_2.

forward and effective approach for promoting the HER efficiency of Mo_2C for high-performance water splitting.

2. Experimental section

2.1. Materials

The commercial molybdenum disulfide (MoS_2, 98 wt%) was purchased from Jinduicheng Molybdenum Industry Co., Ltd. The sodium carbonate (Na_2CO_3, GR, ≥99.8 %), urea (CH_4N_2O AR, ≥99.0 %), hydrochloric acid (HCl AR, 36.0∼38.0 %) and potassium hydroxide (KOH AR, ≥85 %) were purchased from Sinopharm Chemical Reagent Co., Ltd. All the reagents were used as purchased without further purification.

2.2. Synthesis of 2D Mo_2C nanosheets

The precursor mixture of MoS_2, Na_2CO_3, and urea, in a 1:2.5:8 ratio, was homogenized in an agate mortar, loaded into a quartz crucible, and thermally treated at 800 °C for 8 h under an argon/hydrogen (Ar/H_2) atmosphere. Following natural cooling, the resultant material was then treated with 1 M HCl and stirred for 2 h to remove the by-product of sodium disulfide (Na_2S). Finally, the 2D Mo_2C nanosheets were obtained after freeze-drying overnight.

2.3. Synthesis of 2D hetero-structured Mo/Mo_2C nanosheets

The 2D hetero-structured Mo/Mo_2C nanosheets were prepared by annealing the 2D Mo_2C nanosheets precursors at 850 °C for 1, 3, and 5 h under flowing 10 vol% H_2/Ar (100 sccm) at a ramping rate of 5 °C min^{-1} (denoted as Mo/Mo_2C-1, Mo/Mo_2C-3, and Mo/Mo_2C-5, respectively).

2.4. Characterization

Comprehensive characterization included morphological analysis by scanning electron microscopy (SEM, Thermo Fisher/Apreo S HiVac) and transmission electron microscopy (TEM, JEM-2100), and crystallographic profiling by X-ray diffraction (XRD, Rigaku/SmartLab with Cu Kα radiation). The surface electronic structure measurements utilized X-ray photoelectron spectroscopy (XPS, AXIS SUPRA+) and X-ray absorption near-edge spectroscopy (XANES 5–22 keV), while work functions were measurements utilized ultraviolet photoelectron spectroscopy (UPS, Thermo ESCALAB 250XI).

2.5. Electrochemical measurements

Electrochemical analyses were performed using a Biologic VSP-300 workstation. The HER properties were determined via a three-electrode system, where a carbon rod served as the counter electrode and a saturated calomel electrode (SCE) acted as the reference. Catalysts (prepared samples or commercial Pt/C) were uniformly coated onto copper foam as working electrodes at a fixed mass loading of 3 mg cm^{-2}. Linear sweep voltammetry (LSV) polarization curves were acquired at 5 mV s^{-1} scan rates, with potentials converted to the reversible hydrogen electrode (RHE) scale and automated 85 % iR correction. Durability testing involved galvanostatic cycling at 300 mA cm^{-2}, while long-term stability was evaluated through 3,000 cyclic voltammetry (CV) cycles (50 mV s^{-1} scan rate). Electrochemical impedance spectroscopy (EIS) measurements spanned frequencies from 0.01 Hz to 100 kHz with a 5 mV AC amplitude.

3. Results and discussion

The synthesis of the 2D in-plane hetero-structured Mo/Mo_2C nanosheets is illustrated in Fig. 1b. The Mo_2C hetero-structured are synthesized from the bulk MoS_2 precursor (Fig. S1) by Na_2CO_3-assisted heat treatment with urea as the carbon source. The Mo_2C nanosheets are further annealed under Ar/H_2 to produce in-plane Mo/Mo_2C heterojunction nanosheets by partially removing interstitial C atoms. The SEM micrograph in Fig. 2a illustrates Mo_2C nanosheets with lateral dimensions of 1–3 μm and a vertical thickness of 8–10 nm. Fig. S2a shows the X-ray diffraction (XRD) patterns of Mo_2C nanosheets. The diffraction peaks at 34.5°, 38.1°, 39.6°, and 52.3° correspond to the (100), (002), (101), and (102) crystallographic planes of Mo_2C (PDF# 65–8766), respectively. The high resolution transmission electron microscope (HR-TEM) image of the Mo_2C nanosheet in Fig. 2b confirms the lattice fringe spacing of 0.262 nm, attributed to the (100) crystal plane of hexagonal Mo_2C. The atomic force microscopy (AFM) image reveals that the thickness of an individual Mo_2C nanosheet approximates 8.3 nm (Fig. 2c). The 2D Mo/Mo_2C nanosheets inherit the morphology of Mo_2C nanosheets (Fig. 2d). The Mo and Mo_2C phases with abundant heterointerfaces are observed from the HR-TEM image of 2D Mo/Mo_2C nanosheets (Fig. 2e). The well-defined interplanar spacings of 0.262 nm and 0.221 nm are assigned to the (100) crystallographic plane of Mo_2C and the (110) plane of Mo, respectively. Furthermore, it can be seen from the Energy-dispersive X-ray spectroscopy (EDS) images that both Mo and C elements are evenly spread across the Mo/Mo_2C-3 nanosheets (Fig. S3). AFM shows that the Mo/Mo_2C nanosheet has a thickness of 8.2 nm (Fig. 2f), which is similar to that of Mo_2C nanosheets, further boosting the formation of in-plane Mo/Mo_2C heterojunction nanosheets. The XRD patterns of Mo/Mo_2C-1, Mo/Mo_2C-3 and Mo/Mo_2C-5 composites (Fig. 2g and Fig. S2a) show distinct diffraction peaks at 40.5°, 58.6° and 73.7°, which are indexed to the (110), (200) and (211) crystallographic planes of cubic Mo (PDF# 89–5023), revealing that the Mo_2C nanosheets are transformed into Mo/Mo_2C heterojunction nanosheets by thermal annealing Mo_2C under Ar/H_2 by partial removal of interstitial C atom. The intensity of the Mo peaks of Mo/Mo_2C-1, Mo/Mo_2C-3, and Mo/Mo_2C-5 increase gradually with annealing time, indicating more Mo phases are formed with time. The mass ratios of Mo are calculated to be 5.7 %, 11.8 %, and 16.4 % for Mo/Mo_2C-1, Mo/Mo_2C-3, and Mo/Mo_2C-5 nanosheets by XRD Rietveld refinement (Fig. S2). The scanning electron microscopy (SEM) and AFM images show that Mo_2C, Mo/Mo_2C-1, Mo/Mo_2C-3, and Mo/Mo_2C-5 have a similar morphology and provide evidence of the topochemical chemical transition from Mo_2C to Mo/Mo_2C nanosheets (Fig. S4).

X-ray photoelectron spectroscopy (XPS) is utilized to probe the changes in the chemical states during the transition from Mo_2C to Mo/Mo_2C nanosheets. The XPS survey spectrum of Mo_2C nanosheets (Fig. S5a) shows the coexistence of Mo and C in Mo/Mo_2C-3. The XPS analysis of Mo/Mo_2C-3 reveals two characteristic peaks in the high-resolution Mo 3*d* spectrum at binding energies of 228.5 eV and 231.6 eV, which are assigned to the Mo^{2+} in Mo_2C (Fig. S5b). A pair of new peaks at 228.1 and 231.2 eV appear from the Mo/Mo_2C-3 nanosheets, indicating Mo^0 in metal Mo [21,22] and further confirming that Mo_2C is converted into the Mo/Mo_2C heterojunction nanosheets. The weak peaks at 229.2 eV/232.3 eV and 232.7 eV/235.8 eV correspond to Mo^{4+} and Mo^{6+} arising from the surface oxidation of Mo/Mo_2C heterojunction nanosheets. The C 1 *s* spectra of Mo_2C and Mo/Mo_2C-3 show two peaks at 284.6 and 282.9 eV for C-C and C-Mo, respectively (Fig. S5c). The C-Mo bond in Mo/Mo_2C-3 is weaker than that of Mo_2C due to the partial transformation of Mo_2C into Mo.

To obtain more information about the local coordination environment and electronic properties of the Mo atoms in Mo_2C and Mo/Mo_2C-3, the Mo K-edge X-ray absorption near-edge structure (XANES) and extended X-ray absorption fine structure (EXAFS) are analyzed. Fig. 2h shows the Mo K-edge XANES plots of the Mo foil, Mo_2C, and Mo/Mo_2C-3. The K-edge absorption edge of Mo_2C/Mo-3 shifts to lower energies relative to Mo_2C, but closer to that of the Mo foil, showing that the average Mo valence state of Mo in Mo/Mo_2C-3 is between 0 and +2. [23,24] The Fourier transform EXAFS spectrum in Fig. 2i reveals the existence of the Mo-C and Mo-Mo bonds in Mo_2C and Mo/Mo_2C-3. Compared with Mo_2C, the bond length of Mo-C (1.65 Å) in Mo/Mo_2C-3 redshifts, whereas the bond length of Mo-Mo (2.62 Å) blueshifts.[25]

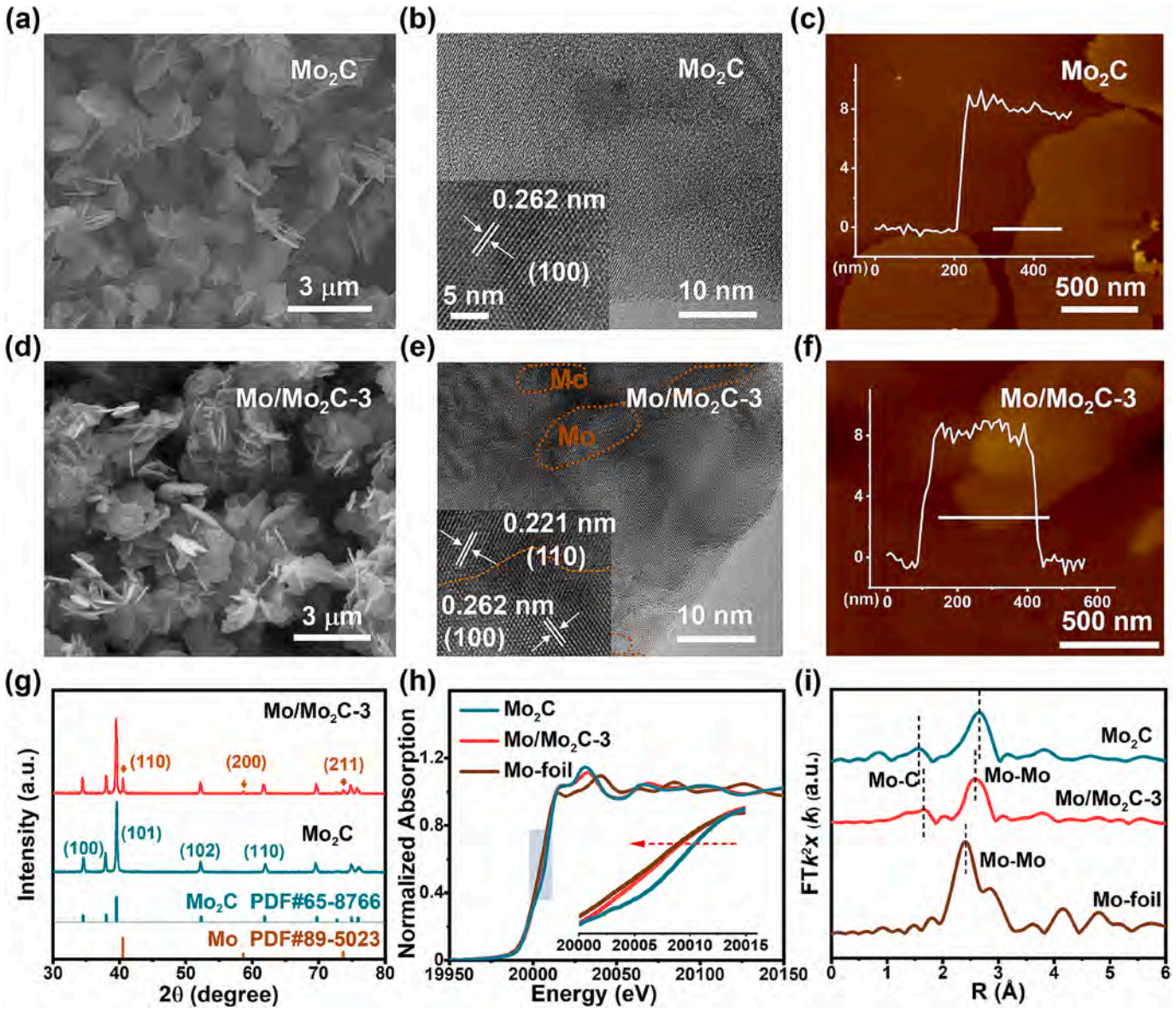

Fig. 2. Morphology, structure, and composite of 2D Mo_2C and Mo/Mo_2C nanosheets. (a) SEM, (b) TEM, and (c) AFM images of Mo_2C nanosheets; (d) SEM, (e) TEM, and (f) AFM images of Mo/Mo_2C-3 nanosheets; (g) XRD patterns of Mo_2C and Mo/Mo_2C-3; (h) Mo K-edge XANES spectra and (i) FT-EXAFS curves of the Mo foil, Mo_2C, and Mo/Mo_2C-3. (The data in the figures are estimated through three independent tests).

The wavelet transform-EXAFS (WT-EXAFS) spectra in Fig. S6 show that the center position of the Mo-Mo bond (8.73 $Å^{-1}$) of Mo/Mo_2C-3 is between those of the Mo foil (8.44 $Å^{-1}$) and Mo_2C (9.25 $Å^{-1}$), further confirming the partial conversion of Mo_2C to Mo. Moreover, the intensity of the Mo-C bond of Mo/Mo_2C-3 is lower than that of Mo_2C, indicating that the local and unsaturated coordination of Mo/Mo_2C-3 enhances the electrochemical activity.[9,26].

The HER properties of the 2D in-plane heterostructured Mo/Mo_2C nanosheets are determined in the 1 M KOH electrolytes. The Mo_2C, Mo/Mo_2C, and commercial 20 wt% Pt/C samples with the same areal mass loading of 3 mg cm^{-2} are coated on copper foam for linear scanning voltammetry (LSV). Fig. 3a shows the polarization curves of Mo_2C, Mo/Mo_2C, and commercial 20 wt% Pt/C. The as-synthesized Mo/Mo_2C electrodes exhibit improved HER activity than the pure Mo_2C electrode. The overpotentials of the Mo_2C/Mo-3 are 90 and 162 mV at 10 and 100 mA cm^{-2}, respectively, surpassing those of Mo_2C (163 and 256 mV), Mo/Mo_2C-1 (135 and 251 mV), and Mo/Mo_2C-5 (175 and 270 mV) nanosheets (Fig. S7). Therefore, Mo/Mo_2C-3 is the optimal electrocatalyst and studied systematically subsequently. Fig. 3b compares the overpotentials of Mo_2C, Mo/Mo_2C-3, and Pt/C at different current densities of 10, 100, and 500 mA cm^{-2}. Mo/Mo_2C-3 shows a low overpotential of 280 mV at 500 mA cm^{-2}, which is even less than that of Pt/C (335 mV). The Tafel slope of Mo/Mo_2C-3 is 54.9 mV dec^{-1} and smaller than that of Mo_2C (67.3 mV dec^{-1}) (Fig. 3c), indicating enhanced HER kinetics of Mo/Mo_2C-3. The electrochemical impedance spectroscopy (EIS) plots in Fig. S8 disclose that the charge transfer resistance (R_{ct}) of Mo/Mo_2C-3 is 8.2 Ω, which represents a notable reduction compared to that of Mo_2C (16.3 Ω), further revealing faster interfacial charge transfer. Furthermore, to explore the number of active sites in different catalysts, the electrochemical active surface areas (ECSA) of Mo_2C and Mo_2C/Mo-3 are derived from the double-layer capacitance (C_{dl}) based on the CV curves in the non-Faradaic potentials (Figs. S9a and b). The value of C_{dl} of Mo/Mo_2C-3 is calculated to be 34.2 mF cm^{-2}, which is almost 1.5 times larger than that of Mo_2C (24.5 mF cm^{-2}), suggesting more exposed active sites on the Mo/Mo_2C-3 nanosheets (Fig. S9c). Moreover, in-plane Mo/Mo_2C-3 heterojunction nanosheets have a higher turnover frequency (TOF) of 2.5 s^{-1} at 400 mV, which is much higher than that of Mo_2C (1.5 s^{-1}), meaning

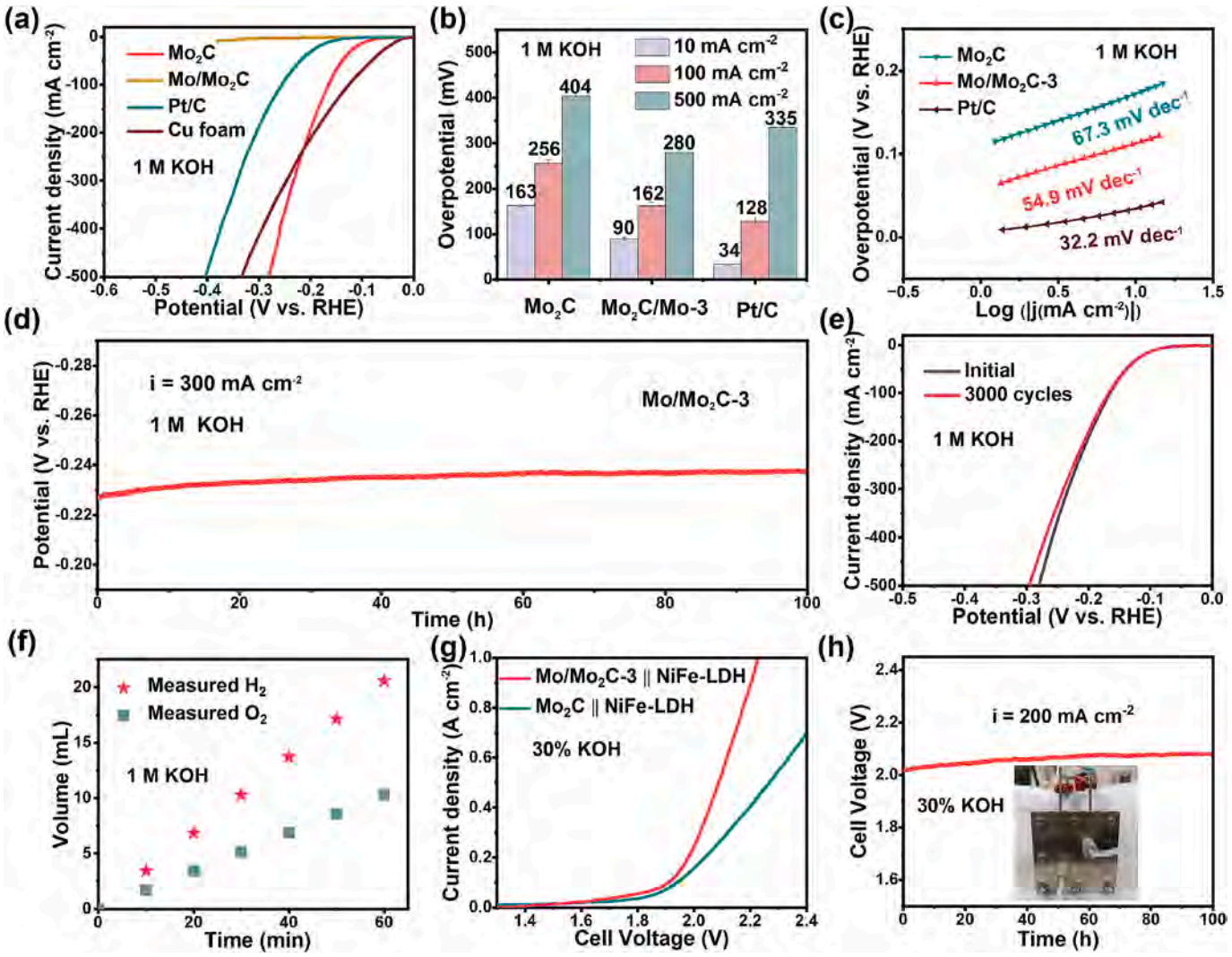

Fig. 3. Electrochemical test results of Mo_2C, Mo/Mo_2C-3 nanosheets and commercial Pt/C electrocatalysts. (a) Polarization curves; (b) Overpotentials after commercial Pt/C in 1 M KOH electrolyte; (d) HER stability test of Mo/Mo_2C-3 at 300 mA cm^{-2} for 100 h; (e) Polarization curves of Mo/Mo_2C-3 before and after 3000 cycles; (f) Faradic efficiency of HER and OER after different measurement (n = 3); (g) Polarization curves for $Mo_2C||$NiFe-LDH and Mo/Mo_2C-3||NiFe-LDH in 30 % KOH electrolyte; (h) Stability test of the AEMWE device at 200 mA cm^{-2} for 100 h. (The data in the figures are estimated through three independent tests).

enhanced intrinsic catalytic activity (Fig. S9d). The galvanostatic test and continuous CV are performed to evaluate the durability of the Mo/Mo_2C-3 electrocatalyst. The potential of the Mo/Mo_2C-3 electrode only increases by ~10 mV at 300 mA cm^{-2} during the operation for 100 h (Fig. 3d). And the LSV curves also exhibit negligible shifts after 3,000 CV cycles (Fig. 3e) to confirm the excellent electrocatalytic stability. The chemical and structural evolution of Mo/Mo_2C-3 after the durability test is monitored by XRD and XPS. Figs. S10–12 disclose that the crystal structure and surface chemical states of Mo/Mo_2C-3 before and after the durability test are almost unchanged, further corroborating the superior electrochemical stability. These results demonstrate that the 2D in-plane Mo/Mo_2C heterojunction nanosheets possess outstanding HER activity performance, matching the benchmark Pt/C catalyst and surpassing other recently developed Mo-based heterostructured electrocatalysts in both overpotentials and Tafel slopes (Table S1).

The HER characteristics of the Mo_2C and Mo/Mo_2C catalysts are also evaluated in an acidic solution. The LSV curve of Mo/Mo_2C-3 in Figures (S13a and b) exhibits overpotentials of 96 and 152 mV at 10 and 100 mA cm^{-2} in 0.5 M H_2SO_4, respectively. They are comparable to those of Pt/C (30 and 125 mV) and superior to those of other recently reported Mo_2C electrocatalysts (Table S2). The corresponding Tafel slope of Mo/Mo_2C-3 is 64.2 mV dec^{-1} (Fig. S13c), which is also smaller than that of Mo_2C (78.2 mV dec^{-1}), suggesting enhanced HER kinetics. The C_{dl} value of the optimal Mo/Mo_2C-3 catalyst is 30.3 mF cm^{-2} in the acidic medium (Fig. S14a–c), which is larger than that of Mo_2C (25.6 mF cm^{-2}). The TOF of Mo/Mo_2C-3 is calculated to be 2.4 s^{-1} at an overpotential of 400 mV, surpassing that of Mo_2C (Fig. S14d). More importantly, the Mo/Mo_2C-3 catalyst has outstanding stability in the acidic solution as exemplified by continuous galvanostatic test results acquired at 100 mA cm^{-2} for 100 h (Fig. S15).

To assess the feasibility of the Mo/Mo_2C electrocatalyst in practical application, an overall water-splitting (OWS) electrolyzer consisting of the NiFe-LDH anode and Mo/Mo_2C cathode is fabricated. The LSV plots in Fig. S16 disclose that the $Mo/Mo_2C||$NiFe-LDH electrolyzer in full water splitting requires only 1.54 and 1.68 V at 10 and 100 mA cm^{-2} in 1 M KOH, which are comparable to those of the Pt/C||RuO_2 electrolyzer (1.54 V and 1.65 V), indicating the high electrocatalytic activity of the $Mo/Mo_2C||$NiFe-LDH electrolyzer. Moreover, the Faradic efficiency of Mo/Mo_2C-3 in HER, which is quantified using a two-electrode configuration at 50 mA cm^{-2} for 60 min, is approximately 99.2 % (Fig. 3f). An anion exchange membrane water electrolyzer (AEMWE) is assembled with the Mo/Mo_2C cathode and NiFe-LDH anode in 30 % KOH (Fig. S17). Fig. 3g shows that the Mo/Mo_2C-3||NiFe-LDH-based OWS cell exhibits a cell voltage of 2.23 V to drive 1,000 mA cm^{-2} at room

temperature, which is much lower than that of $Mo_2C||$NiFe-LDH and outperforms to most previously developed Mo-based overall water-splitting cells. Moreover, Mo/Mo_2C-3 exhibits excellent long-term stability during OWS at 200 mA cm^{-2} for 100 h (Fig. 3h).

The water contact angles are measured to characterize the hydrophilicity, which is crucial in the adsorption of H_2O and the motion of H_2 bubbles.[10,27] The water contact angle on Mo/Mo_2C-3 is close to 19°, which is much smaller than that on Mo_2C of 77°, demonstrating enhanced water adsorption (Fig. 4a and b). The real-time surfaces on the Mo_2C and Mo/Mo_2C-3 electrodes are recorded (Videos S1 and S2). Many large H_2 bubbles (~500 μm in diameter) adsorb to the surface of the Mo_2C electrode and obscure the active sites on the Mo_2C catalyst, thereby reducing the HER kinetics. In contrast, the H_2 bubbles are much smaller on the surface of Mo/Mo_2C-3 due to enhanced H desorption and HER activity after the introduction of Mo into the Mo_2C nanosheets.

To understand the underlying mechanism of the improved HER activity of the 2D Mo/Mo_2C heterojunction nanosheets, the band structure and the interfacial electron interaction between Mo and Mo_2C are studied by ultraviolet photoelectron spectroscopy in conjunction with DFT calculations. The values of the work functions for Mo_2C and Mo are 5.31 eV and 5.01 eV, respectively (Fig. S18). The difference in the work functions drives electron migration from Mo to Mo_2C at the Mo/Mo_2C interface until equilibrium, as schematically shown in Fig. 5a and b. The interfacial electron redistribution is further investigated by density-functional theory (DFT) calculations based on the optimized structure of the Mo (110) and Mo_2C (100) systems (Figs. S19 and S20). The charge density difference map in Fig. 5c shows that electron transfer from Mo to Mo_2C enriches electrons at the Mo sites of Mo_2C at the heterointerface, thereby ultimately optimizing the electronic structure of heterointerface Mo active sites to enhance HER kinetics. The partial density of states (PDOS) distributions of Mo, Mo/Mo_2C, and Mo_2C are derived to illustrate the interactions between the H* species and Mo sites. Fig. 5d discloses that the *d* band center (E_d) relative to the Fermi level (E_F) of the Mo site in Mo_2C is −1.46 eV which is closer to E_F than that of Mo (−1.98 eV), revealing the high Mo-H binding energy in Mo_2C. However, E_d of the Mo site at the Mo/Mo_2C interface downshifts from −1.46 eV to −1.62 eV, suggesting that the Mo-H binding energy declines after the integration of Mo into Mo_2C.[28] When hydrogen adsorbs at Mo atoms on Mo/Mo_2C, the formation of H 1*s*-Mo 4*d* hybrid orbital exhibits an increased occupancy of the antibonding orbital state than that on Mo_2C according to the *d*-band theory, leading to the reduced H-binding energy.[28] Moreover, the PDOS of the active Mo atoms at the Mo/Mo_2C interface near E_F is the highest (Fig. S21), thus favoring the adsorption and dissociation of H_2O molecules [10]. As indicated in Fig. 5e, the water adsorption energy at the Mo site of the Mo/Mo_2C heterointerface is calculated to be −0.38 eV, which is lower than those at Mo (110) of 0.16 eV and Mo_2C (100) of −0.21 eV, revealing more favorable water adsorption at the Mo/Mo_2C interface. The energy barrier for OH-H bond cleavage at the Mo/Mo_2C heterojunction is calculated to be 0.53 eV, which is less than those on bare Mo (0.92 eV) and Mo_2C (0.66 eV), respectively, implying improved water dissociation at the Mo/Mo_2C interface (Fig. 5f). Moreover, the interfacial Mo site of the Mo/Mo_2C heterojunction shows a more favorable hydrogen adsorption free energy (ΔG_{H^*}) of −0.14 eV than Mo (0.33 eV) and Mo_2C (−0.56 eV), confirming that the interfacial Mo site serves as the active site to achieve efficient HER (Fig. 5g). The above results reveal that the formation of the Mo/Mo_2C heterojunction gives rise to electron migration from Mo to Mo_2C and increases the antibonding-orbital occupancy state for the H 1*s*-Mo 4*d* hybrid orbital, which downshifts the E_d, weakens Mo-H, and achieves efficient hydrogen evolution (Fig. 5h). All in all, the Mo/Mo_2C heterojunction facilitates water adsorption/dissociation and shows the optimal hydrogen adsorption/desorption behavior as well as HER activity and kinetics.

4. Conclusion

In summary, a high-performance two-dimensional in-plane Mo/Mo_2C heterojunction nanosheet catalyst for hydrogen evolution reaction is prepared from bulk MoS_2 via the molten salt-assisted technique, followed by annealing under Ar/H_2 to partially remove interstitial carbon atoms. This tunable and non-destructive topochemical transition can effectively circumvent the issues of insufficient modification caused by low atomic doping concentrations and the unavoidable structural damage of nanosheets induced by dopant atoms. Density-functional theory calculations and experiments results reveal that the Mo/Mo_2C possesses several advantages in this study: i) the unique 2D in-plane structure yields enriched active sites, enables fast H_2O adsorption, and promotes mass transfer for efficient release of H_2 bubbles; ii) the electron migration in the in-plane heterointerface downshifts the d-band center, increases the antibonding-orbital occupancy state of Mo_2C, weakens the Mo-H bonding to optimize the H adsorption/desorption, and enhances the HER kinetics of the Mo/Mo_2C heterojunction; iii) the composition ratio of Mo/Mo_2C could be optimized via adjusting the reduction time in the Ar/H_2 ambient. As a result, the optimal Mo/Mo_2C possesses low overpotentials of 90 and 96 mV at 10 mA cm^{-2} and small Tafel slopes of 54.9 and 64.2 mV dec^{-1} in alkaline and acidic media. The

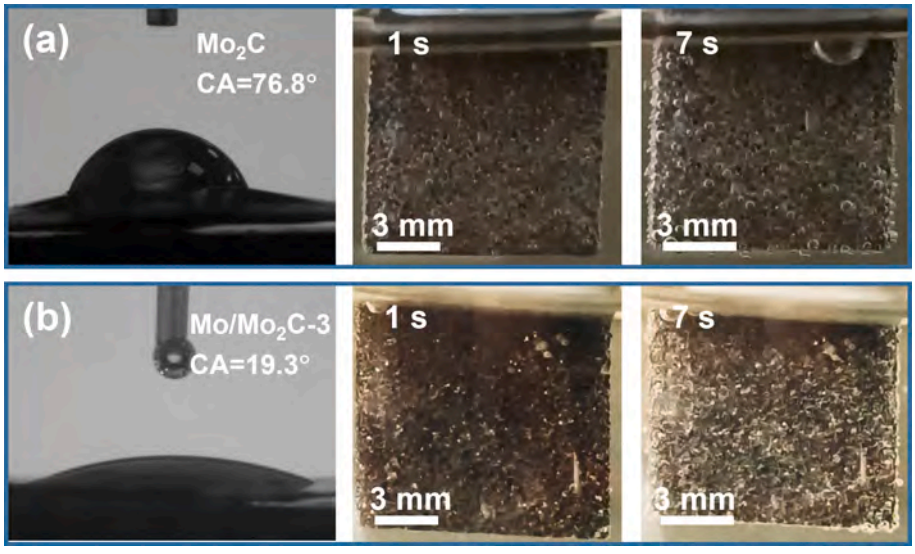

Fig. 4. Contact angle measurement after different measurement (n = 3) and H_2 bubble evolution: (a) Mo_2C and (b) Mo/Mo_2C-3.

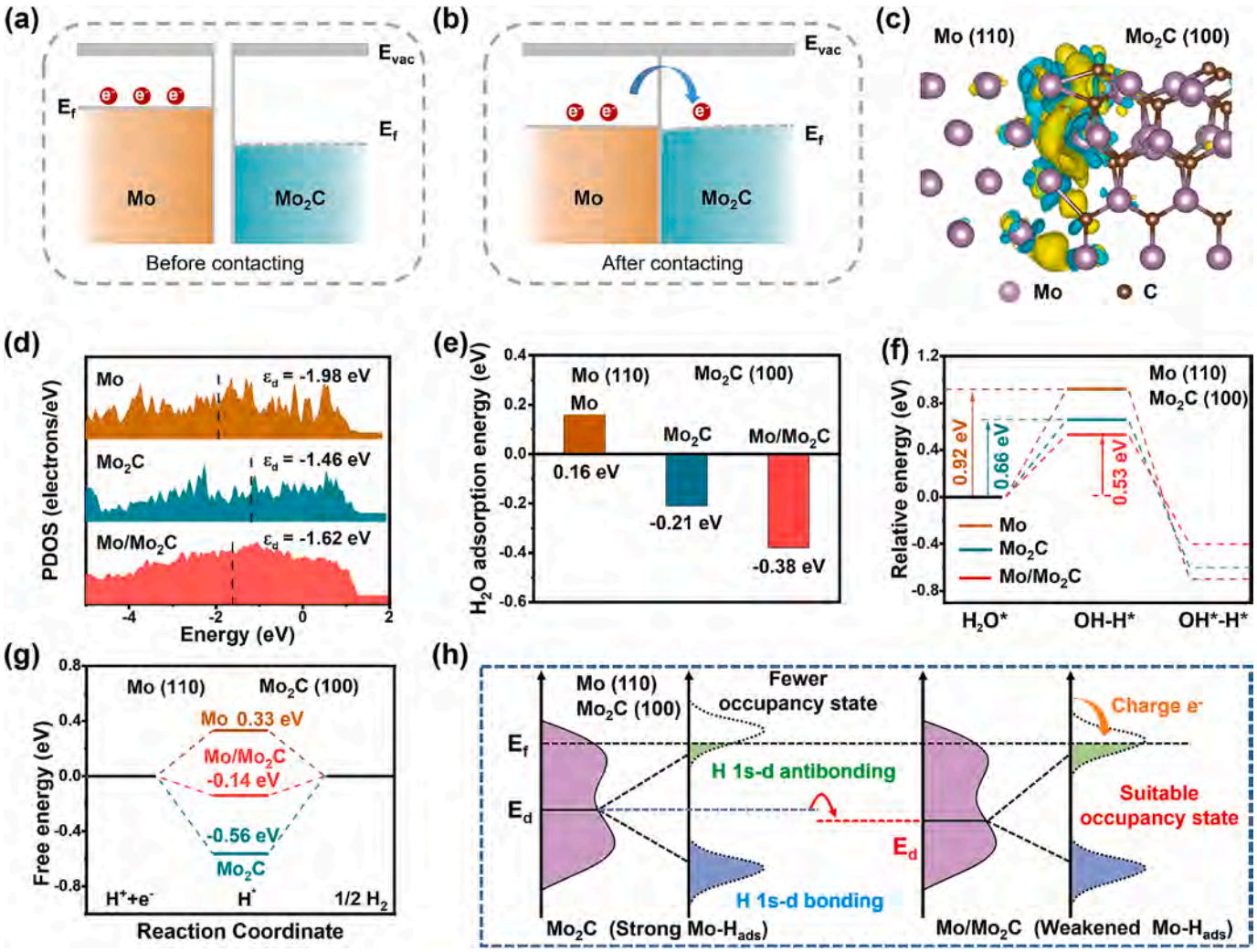

Fig. 5. Schematics of the band structure and theoretical results of Mo/Mo_2C: (a and b) Energy band schematics of Mo, Mo_2C, and in-plane Mo/Mo_2C heterointerface (E_{vac} represents the vacuum level, E_f is the Fermi level); (c) Charge density difference map at the Mo/Mo_2C heterointerface. The yellow and blue isosurfaces represent charge accumulation and depletion, respectively; (d) DOS of Mo 4*d* and corresponding *d*-band centers of Mo, Mo_2C, and Mo/Mo_2C; (e) H_2O adsorption energy, (f) Dissociation barrier for H_2O molecule, and (g) Gibbs free energies of H* on Mo atoms at the Mo, Mo_2C, and Mo/Mo_2C interfaces; (h) Schematic illustration of the weakened Mo-H_{ads} bond by increasing antibonding-orbital occupancy state of Mo at heterointerface. (For interpretation of the references to colour in this figure legend, the reader is referred to the web version of this article.)

Mo/Mo_2C only requires an overpotential of 280 mV to attain 500 mA cm^{-2} in the alkaline electrolyte, surpassing those of the benchmark Pt/C and many Mo_2C-based catalysts recently reported. This work provides new insights into the rational design of 2D in-plane heterostructure to boost the HER activity of transition metal carbides in water splitting.

CRediT authorship contribution statement

Yulei Ren: Writing – original draft, Methodology, Investigation, Data curation. **Rui Huo:** Investigation, Formal analysis. **Xiuli Li:** Methodology, Data curation. **Hao Song:** Investigation, Formal analysis, Data curation. **Xuming Zhang:** Investigation, Formal analysis. **Biao Gao:** Resources, Investigation. **Paul K. Chu:** Writing – review & editing, Investigation. **Kaifu Huo:** Writing – review & editing, Supervision, Project administration, Funding acquisition, Conceptualization.

Declaration of competing interest

The authors declare that they have no known competing financial interests or personal relationships that could have appeared to influence the work reported in this paper.

Acknowledgements

This work was financially supported by the National Natural Science Foundation of China (Nos. U2004210, U2003130, and 22379116), Shenzhen Science and Technology Program (JCYJ20210324141613032), Outstanding Youth Foundation of Natural Science Foundation of Hubei Province (2020CFA099), Key Research and Development Program of Hubei Province (2021BAA176 and 2021BAA208), and City University of Hong Kong Donation Research Grants (DON-RMG 9229021 and 9229061). The authors are grateful to the facility support provided by the Analytical and Testing Center of Huazhong University of Science and Technology and the Analytical and Testing Center of Wuhan University of Science and Technology.

Appendix A. Supplementary data

Supplementary data to this article can be found online at https://doi.org/10.1016/j.jcis.2025.137400.

Data availability

Data will be made available on request.

References

[1] X. Liu, Y. Yu, K. Li, Y. Li, X. Li, Z. Yuan, H. Li, H. Zhang, M. Gong, W. Xia, Y. Deng, W. Lei, Intergrating hollow multishelled structure and high entropy engineering toward enhanced mechano-electrochemical properties in lithium battery, Adv. Mater. 2312583 (2024).

[2] H. Yu, D. Wang, H. Jin, P. Wu, X. Wu, D. Chu, Y. Lu, X. Yang, H. Xu, 2D $MoN_{1.2-r}GO$ stacked heterostructures enabled water state modification for highly efficient interfacial solar evaporation, Adv. Funct. Mater. 33 (2023) 2214828.

[3] L. Guo, J. Chi, J. Zhu, T. Cui, J. Lai, L. Wang, Dual-doping $NiMoO_4$ with multi-channel structure enable urea-assisted energy-saving H_2 production at large current density in alkaline seawater, Appl. Catal. b: Environ. 320 (2023) 121977.

[4] P. Yang, F. Liu, X. Zang, L. Xin, W. Xiao, G. Xu, H. Li, Z. Li, T. Ma, J. Wang, Z. Wu, L. Wang, Microwave quasi-solid state to construct strong metal-support interactions with interfacial electron-enriched Ru for anion exchange membrane electrolysis, Adv. Energy Mater. 14 (2024) 2303384.

[5] H. Su, X. Pan, S. Li, H. Zhang, R. Zou, Defect-engineered two-dimensional transition metal dichalcogenides towards electrocatalytic hydrogen evolution reaction, Carbon Energy 5 (2023) 296.

[6] L. Li, S. Liu, C. Zhan, Y. Wen, Z. Sun, J. Han, T.-S. Chan, Q. Zhang, Z. Hu, X. Huang, Surface and lattice engineered ruthenium superstructures towards high-performance bifunctional hydrogen catalysis, Energy & Environ. Sci. 16 (2023) 157–166.

[7] J. Wei, K. Xiao, Y. Chen, X.-P. Guo, B. Huang, Z.-Q. Liu, In situ precise anchoring of Pt single atoms in spinel Mn_3O_4 for a highly efficient hydrogen evolution reaction, Energy & Environ. Sci. 15 (2022) 4592–4600.

[8] C. Pi, C. Huang, Y. Yang, H. Song, X. Zhang, Y. Zheng, B. Gao, J. Fu, P.K. Chu, K. Huo, In situ formation of N-doped carbon-coated porous MoP nanowires: a highly efficient electrocatalyst for hydrogen evolution reaction in a wide pH range, Appl. Catal. b: Environ. 263 (2020) 118358.

[9] C. Yang, K. Shen, R. Zhao, H. Xiang, J. Wu, W. Zhong, Q. Zhang, X. Li, N. Yang, Balance effect: a universal strategy for transition metal carbides to enhance hydrogen evolution, Adv. Funct. Mater. 32 (2022) 2108167.

[10] W. Liu, X. Wang, F. Wang, K. Du, Z. Zhang, Y. Guo, H. Yin, D. Wang, A durable and pH-universal self-standing MoC-Mo_2C heterojunction electrode for efficient hydrogen evolution reaction, Nat. Commun. 12 (2021) 6776.

[11] W. Zhang, L. Yang, Z. Li, G. Nie, X. Cao, Z. Fang, X. Wang, S. Ramakrishna, Y. Long, L. Jiao, Regulating hydrogen/oxygen species adsorption via built-in electric field-driven electron transfer behavior at the heterointerface for efficient water splitting, Angew. Chem. Int. Edi. 63 (2024) e202400888.

[12] M. Sher Shah, G. Jang, K. Zhang, J. Park, Transition metal carbide-based nanostructures for electrochemical hydrogen and oxygen evolution reactions, EcoEnergy 1 (2023) 344–374.

[13] X. Lang, M.A. Qadeer, G. Shen, R. Zhang, S. Yang, J. An, L. Pan, J.-J. Zou, A Co-Mo_2N composite on a nitrogen-doped carbon matrix with hydrogen evolution activity comparable to that of Pt/C in alkaline media, J. Mater. Chem. A 7 (2019) 20579–20583.

[14] X. Zhang, T. Liu, T. Guo, Z. Mu, X. Hu, K. He, X. Chen, V.P. Dravid, Z. Wu, D. Wang, High-performance MoC electrocatalyst for hydrogen evolution reaction enabled by surface sulfur substitution, ACS Appl. Mater. Interfaces 13 (2021) 40705–40712.

[15] B. Gao, Y. Huang, S. Wang, H. Lu, L. Zheng, X. Fan, X. Yang, W. Zhang, Y. Wang, Y. Zhang, Q. Gao, Y. Tang, MoC nanodots toward efficient electrocatalytic hydrogen evolution: an interlayer-confined strategy with a 2D-zeolite precursor, J. Mater. Chem. A 9 (2021) 4724–4733.

[16] Y. Wang, W. Hong, C. Jian, X. He, Q. Caia, W. Liu, The intrinsic hydrogen evolution performance of 2D molybdenum carbide, J. Mater. Chem. A 8 (2020) 24204–24211.

[17] M. Pan, P. Wang, X. Wang, F. Chen, H. Yu, Weakening Mo-H bond of Mo_2C Mxene cocatalyst by increased antibonding-orbital occupancy state for superior photocatalytic hydrogen production, ACS Sustain. Chem. Eng. 11 (2023) 13222–13231.

[18] C. Yang, R. Zhao, H. Xiang, J. Wu, W. Zhong, X. Li, Q. Zhang, Structural transformation of molybdenum carbide with extensive active centers for superior hydrogen evolution, Nano Energy 98 (2022) 107232.

[19] Z. Liu, H. He, Y. Liu, Y. Zhang, J. Shi, J. Xiong, S. Zhou, J. Li, L. Fan, W. Cai, Soft-template derived Ni/Mo_2C hetero-sheet arrays for large current density hydrogen evolution reaction, J. Colloid Interface Sci. 635 (2023) 23–31.

[20] T. Wang, P. Wang, Y. Pang, Y. Wu, J. Yang, H. Chen, X. Gao, S. Mu, Z. Kou, Vertically mounting molybdenum disulfide nanosheets on dimolybdenum carbide nanomeshes enables efficient hydrogen evolution, Nano Res. 15 (2022) 3946–3951.

[21] J. Xiong, J. Li, J. Shi, X. Zhang, N.-T. Suen, Z. Liu, Y. Huang, G. Xu, W. Cai, X. Lei, L. Feng, Z. Yang, L. Huang, H. Cheng, In situ engineering of double-phase interface in Mo-Mo_2C heteronanosheets for boosted hydrogen evolution reaction, ACS Energy Lett. 3 (2018) 341–348.

[22] C. Wu, G. Qi, J. Zhang, J. Cheng, B. Wang, Porous Mo_3P/Mo nanorods as efficient mott-schottky cathode catalysts for low polarization Li-CO_2 battery, Small 19 (2023) 2302078.

[23] C. Pi, X. Li, X. Zhang, H. Song, Y. Zheng, B. Gao, A. Kizilaslan, P.K. Chu, K. Huo, In-plane mott-schottky effects enabling efficient hydrogen evolution from Mo_5N_6-MoS_2 heterojunction nanosheets in universal-pH electrolytes, Small 18 (2022) e2201137.

[24] Z. Wu, Q. Li, G. Xu, W. Jin, W. Xiao, Z. Li, T. Ma, S. Feng, L. Wang, Microwave phosphine-plasma-assisted ultrafast synthesis of halogen-doped Ru/RuP_2 with surface intermediate adsorption modulation for efficient alkaline hydrogen evolution reaction, Adv. Mater. 36 (2024) 2311018.

[25] D. Li, R. Cai, D. Zheng, J. Ren, C.L. Dong, Y.C. Huang, S.J. Haigh, X. Liu, F. Gong, Y. Liu, J. Liu, D. Yang, A sustainable route to ruthenium phosphide (RuP)/Ru heterostructures with electron-shuttling of interfacial Ru for efficient hydrogen evolution, Adv. Sci. 2309869 (2024).

[26] Z. Chen, W. Gong, J. Wang, S. Hou, G. Yang, C. Zhu, X. Fan, Y. Li, R. Gao, Y. Cui, Metallic W/WO_2 solid-acid catalyst boosts hydrogen evolution reaction in alkaline electrolyte, Nat. Commun. 14 (2023) 5363.

[27] W. Liu, X. Wang, J. Qu, X. Liu, Z. Zhang, Y. Guo, H. Yin, D. Wang, Tuning Ni dopant concentration to enable co-deposited superhydrophilic self-standing Mo_2C electrode for high-efficient hydrogen evolution reaction, Appl. Catal. b: Environ. 307 (2022) 121201.

[28] L. Dai, F. Yao, Yu. Lei, C. Fang, J. Li, L. Xue, S. Zhang, P. Xiong, Y. Fu, J. Sun, J. Zhu, Boosting alkaline hydrogen evolution on stoichiometric molybdenum carbonitride via an interstitial vacancy-elimination strategy, Adv. Energy Mater. 12 (2022) 2200974.

Supporting Information

Controllable Synthesis of In-Plane Mo/Mo_2C Heterojunction Nanosheets for Enhanced Hydrogen Evolution Reaction

Yulei Ren [a, b], Rui Huo [e], Xiuli Li [a], Hao Song [a, *], Xuming Zhang [a], Biao Gao [a], Paul K. Chu [c], and Kaifu Huo [b, d*]

[a] State Key Laboratory of Advanced Refractories, Institute of Advanced Materials and Nanotechnology, Wuhan University of Science and Technology, Wuhan 430081, China

[b] Wuhan National Laboratory for Optoelectronics (WNLO), School of Optical and Electronic Information, Huazhong University of Science and Technology, Wuhan 430074, China

[c] Department of Physics, Department of Materials Science and Engineering, and Department of Biomedical Engineering, City University of Hong Kong, Tat Chee Avenue, Kowloon, Hong Kong, China

[d] Research Institute of Huazhong University of Science and Technology in Shenzhen, Shenzhen 518063, China

[e] School of Materials and Engineering, Central South University, Changsha 410083, China

*Corresponding authors: E-mail: songhao201809@wust.edu.cn (H. Song); kfhuo@hust.edu.cn (K.F. Huo)

Yulei Ren, and Rui Huo contributed equally to this work.

The Turnover Frequency Calculations (TOF$_s$) can be calculated by the following equation:

$$\mathrm{TOF} = \frac{\text{the number of total hydrogen turnovers per cm}^2}{\text{the number of active sites per cm}^2}$$

The number of total hydrogen turnovers per cm^2 is equal to:

$$\left(\mathrm{j}\frac{\mathrm{mA}}{\mathrm{cm}^2}\right)\left(\frac{1\,\mathrm{C\,s^{-1}}}{1000\,\mathrm{mA}}\right)\left(\frac{1\,\mathrm{mol\ of\ e^-}}{96485.3\,\mathrm{C}}\right)\left(\frac{1\,\mathrm{mol\ of\ H_2}}{2\,\mathrm{mol\ of\ e^-}}\right)\left(\frac{6.022\times10^{23}\,\mathrm{H_2\ molecules}}{1\,\mathrm{mol\ of\ H_2}}\right)$$

$$= 3.12\times10^{15}\,\frac{\mathrm{H_2/s}}{\mathrm{cm}^2}\times|\mathrm{j}|$$

The unit cell of Mo metal contains two Mo atoms with a volume of 31.11 Å^{3,} and Mo_2C contains two Mo atoms with a volume of 36.7 Å^3. Considering that Mo/Mo_2C is composed of mixed Mo and Mo_2C, the number of active sites is related to the relative content of each phase derived from the XRD quantitative analysis. The number of Mo (or Mo_2C) active sites per cm^2 is equal to the number of Mo (or Mo_2C) active sites per real surface area × ECSA

The double-layer capacitance (C_{dl}) can be calculated by the following equation:

$$\Delta j = \nu C_{dl}$$

where ν is the scan rate and Δj is half of the current density difference in the CV curve ($\Delta j = (j_a - j_c)/2$).

The electrochemically active surface area (ECSA) is linearly related to C_{dl}, and ECSA can be deduced from C_{dl} using the following equation:

$$ECSA = C_{dl} / C_s$$

where C_s represents the specific capacitance per unit area of surface under certain conditions.

The Faradaic Efficiency (η_F) can be calculated by the following equation:

$$\eta_F = \frac{m \times n \times F}{I \times t} \times 100\%$$

where m, n, F, I and t are the molar amount of the relevant product, number of electrons transferred in the reaction, Faraday's constant (96485 C mol-1), average current density and reaction time, respectively.

Density-functional theory (DFT) calculation

DFT calculations were conducted by the Vienna Ab initio Simulation Package (VASP) code and the Perdew-Burke-Eznerhof (PBE) function operation. The interaction between ions and electrons was treated by employing the projector-augmented wave (PAW) method. The plane wave termination energy was set to 500 eV until the strength and energy converged to within 0.02 eV/Å and 10^{-5} eV for each atom. The slab models of Mo (110), Mo_2C (100), and Mo (110)/Mo_2C (100) heterojunction were constructed

according to the high-resolution transmission electron microscopy (HR-TEM) results. The Gibbs free energy was corrected by the formula:

$$\Delta G_{H^*} = \Delta E + \Delta ZPE - T\Delta S$$

where ΔZPE is the energy of zero-point and ΔS is the entropic change (T set to 298 K), respectively.

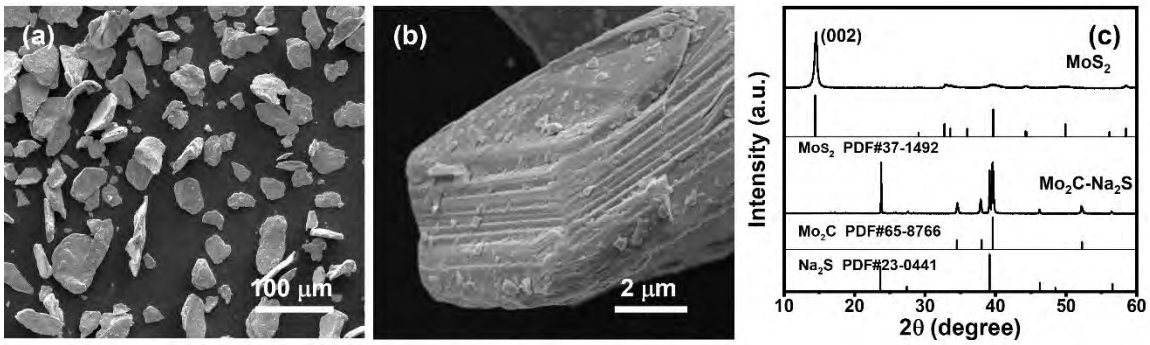

Figure S1. (a, b) SEM images of bulk MoS_2, (c) the XRD patterns of bulk MoS_2 and the product after the molten salt-assisted synthesis.

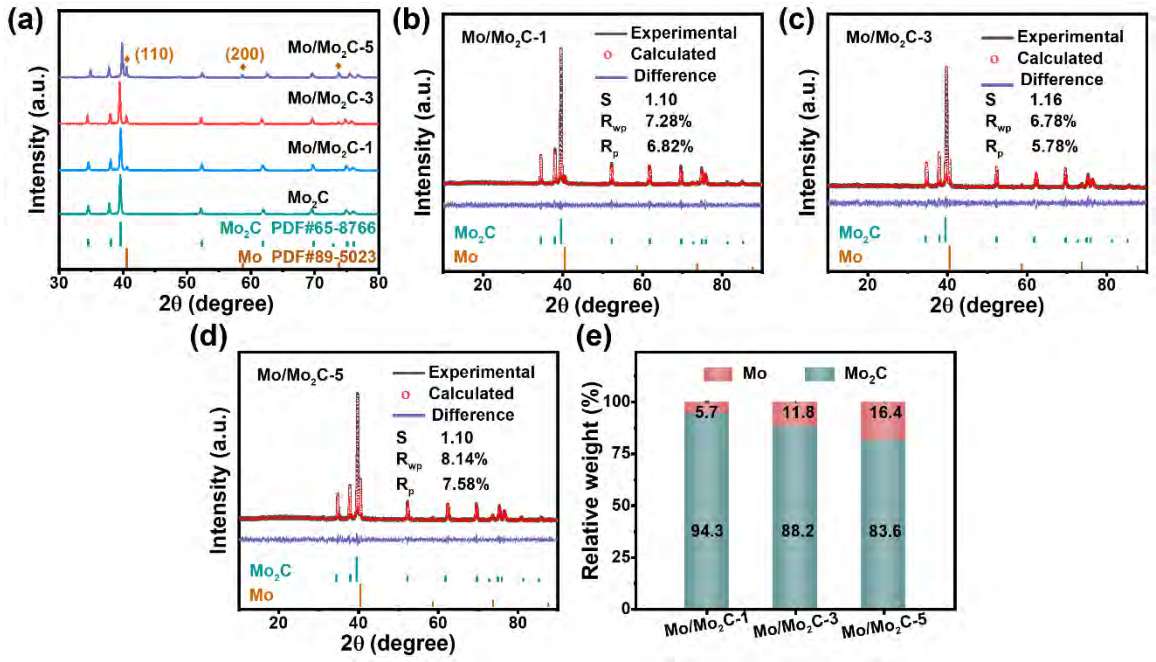

Figure S2. (a) XRD patterns of Mo_2C, Mo/Mo_2C-1, Mo/Mo_2C-3, and Mo/Mo_2C-5; (b-d) XRD Rietveld refinement analysis of Mo/Mo_2C-1, Mo/Mo_2C-3, and Mo/Mo_2C-5; (e) Corresponding relative weights of Mo and Mo_2C by Rietveld refinement analysis after repeated fitting (n = 3).

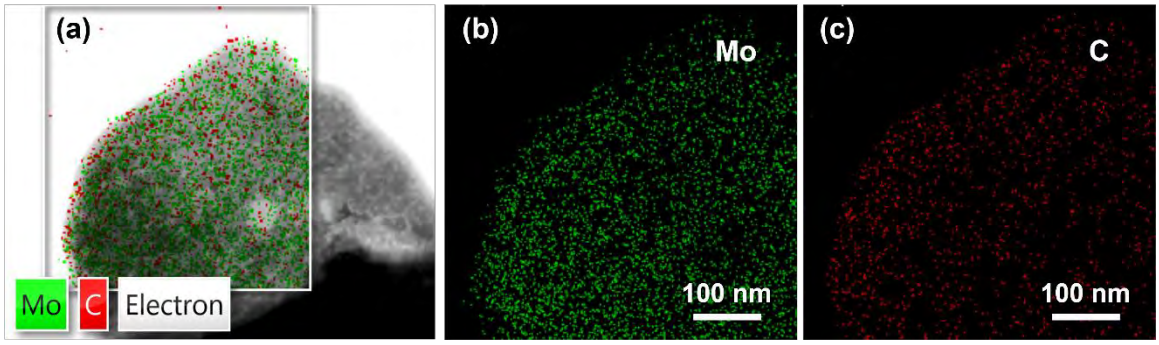

Figure S3. (a) EDS Mapping of Mo/Mo_2C NSs, (b) Mo and (c) C element.

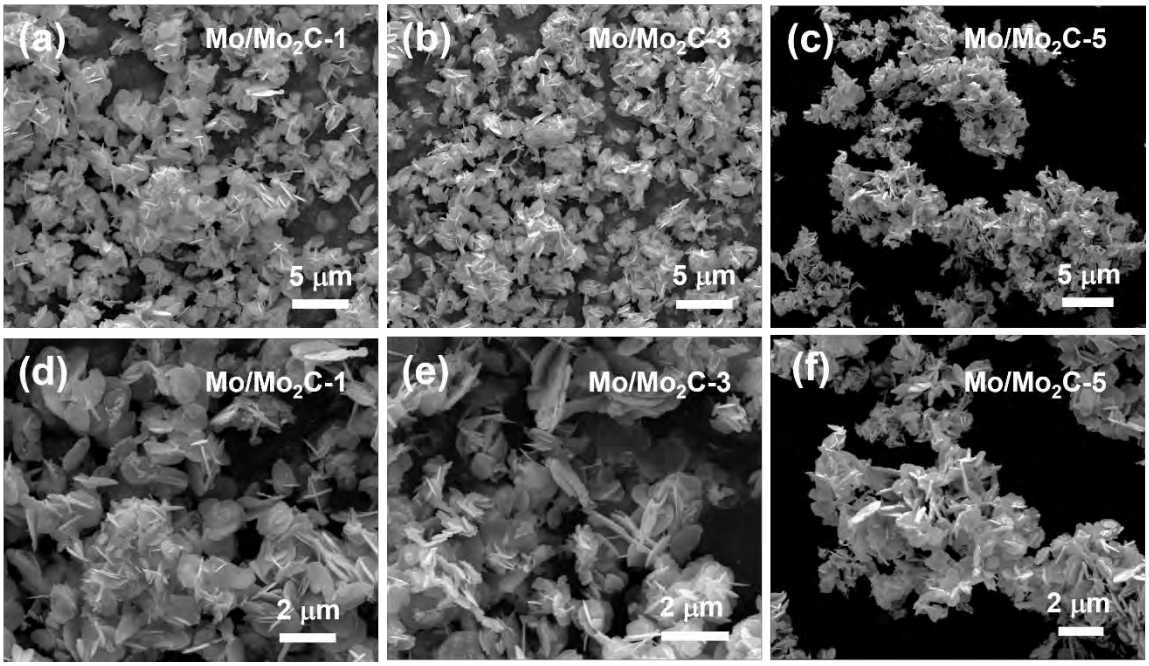

Figure S4. SEM images of (a, d) Mo/Mo_2C-1, (b, e) Mo/Mo_2C-3, and (c, f) Mo/Mo_2C-5 NSs.

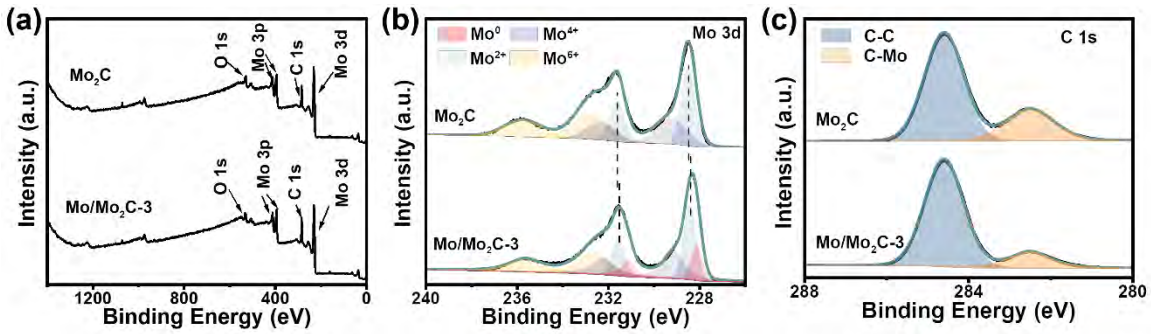

Figure S5. (a) XPS survey spectra of Mo_2C and Mo/Mo_2C-3; High-resolution XPS spectra of Mo_2C and Mo/Mo_2C-3: (b) Mo 3*d* and (c) C 1*s*.

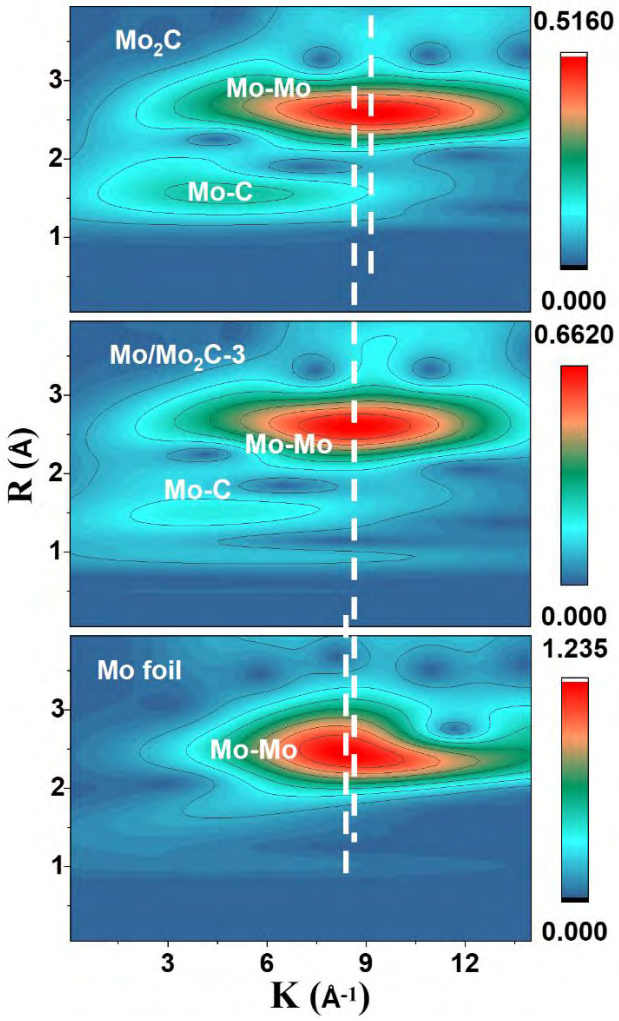

Figure S6. The wavelet transform-EXAFS (WT-EXAFS) of Mo foil, Mo_2C, and Mo/Mo_2C-3.

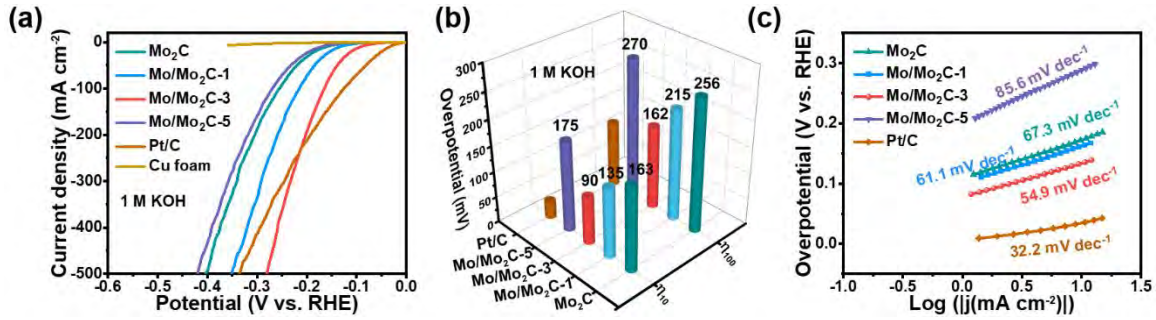

Figure S7. (a) LSV curves and (b) Overpotentials at 10 and 100 mA cm^{-2} of Mo_2C, Mo/Mo_2C-1, Mo/Mo_2C-3, Mo/Mo_2C-5, and Pt/C in 1 M KOH after different measurement (n = 3); (c) Corresponding Tafel plots in 1 M KOH. (Error estimates through three times of independent tests).

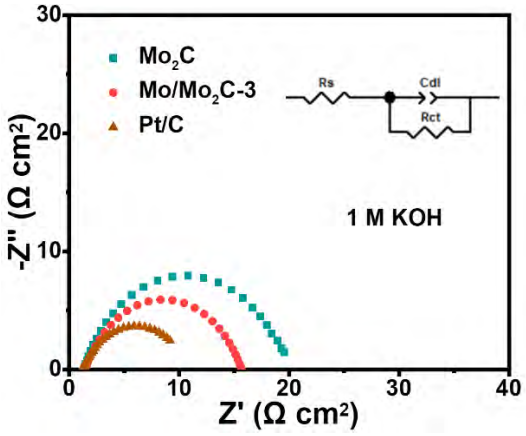

Figure S8. Nyquist plots of Mo_2C, Mo/Mo_2C-3, and Pt/C at open circuit potential corresponding to 10 mA cm^{-2} in 1 M KOH. (Error estimates through three times of independent tests).

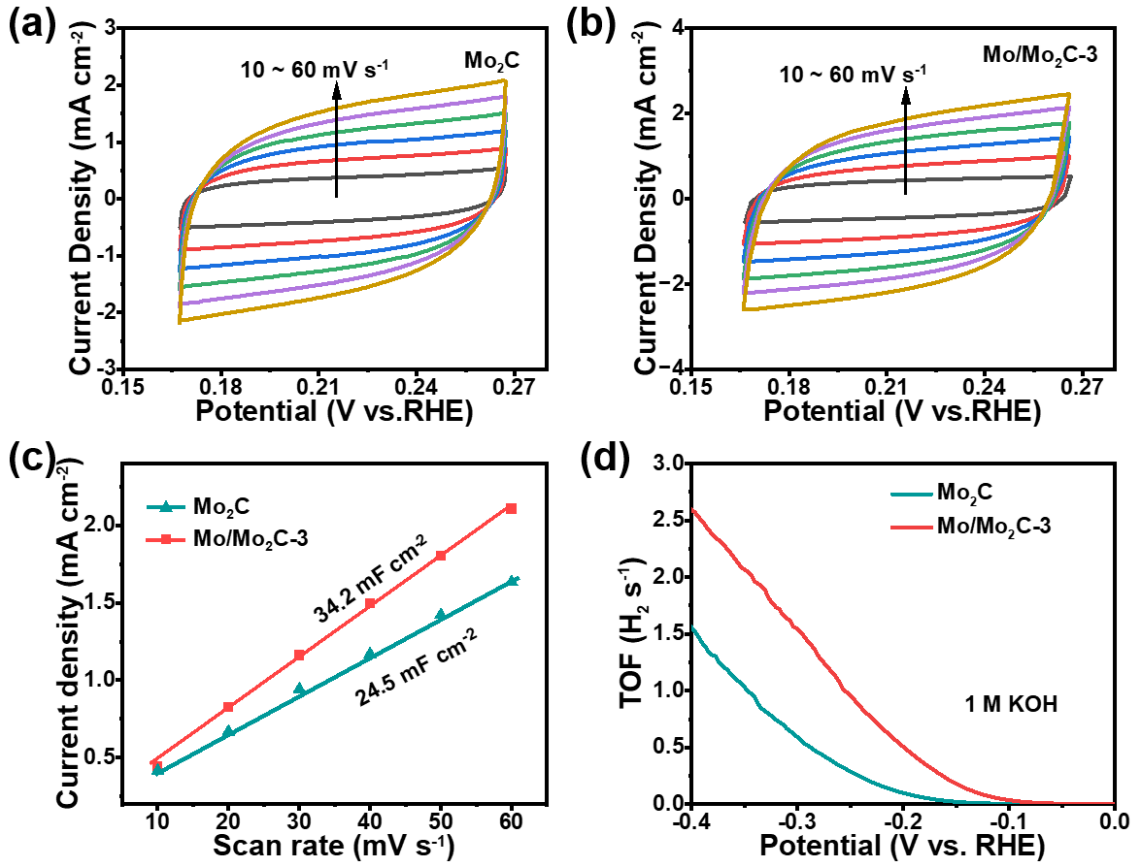

Figure S9. CV curves of (a) Mo_2C and (b) Mo/Mo_2C-3 at different scanning rates from 10 to 60 mV s^{-1} in 1 M KOH; (c) Corresponding double-layer capacitance (C_{dl}) and (d) TOF plots in 1 M KOH. (Error estimates through three times of independent tests).

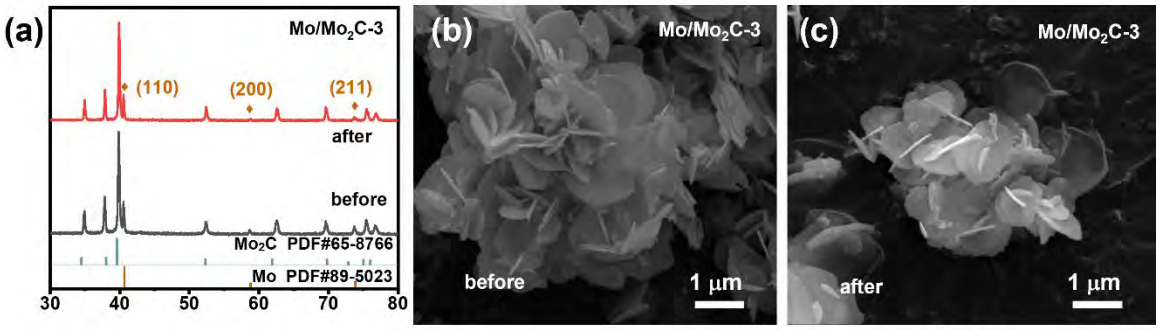

Figure S10. (a) XRD patterns of Mo/Mo_2C-3 before and after the HER durability test; SEM images (b) Before and (c) After the HER durability test.

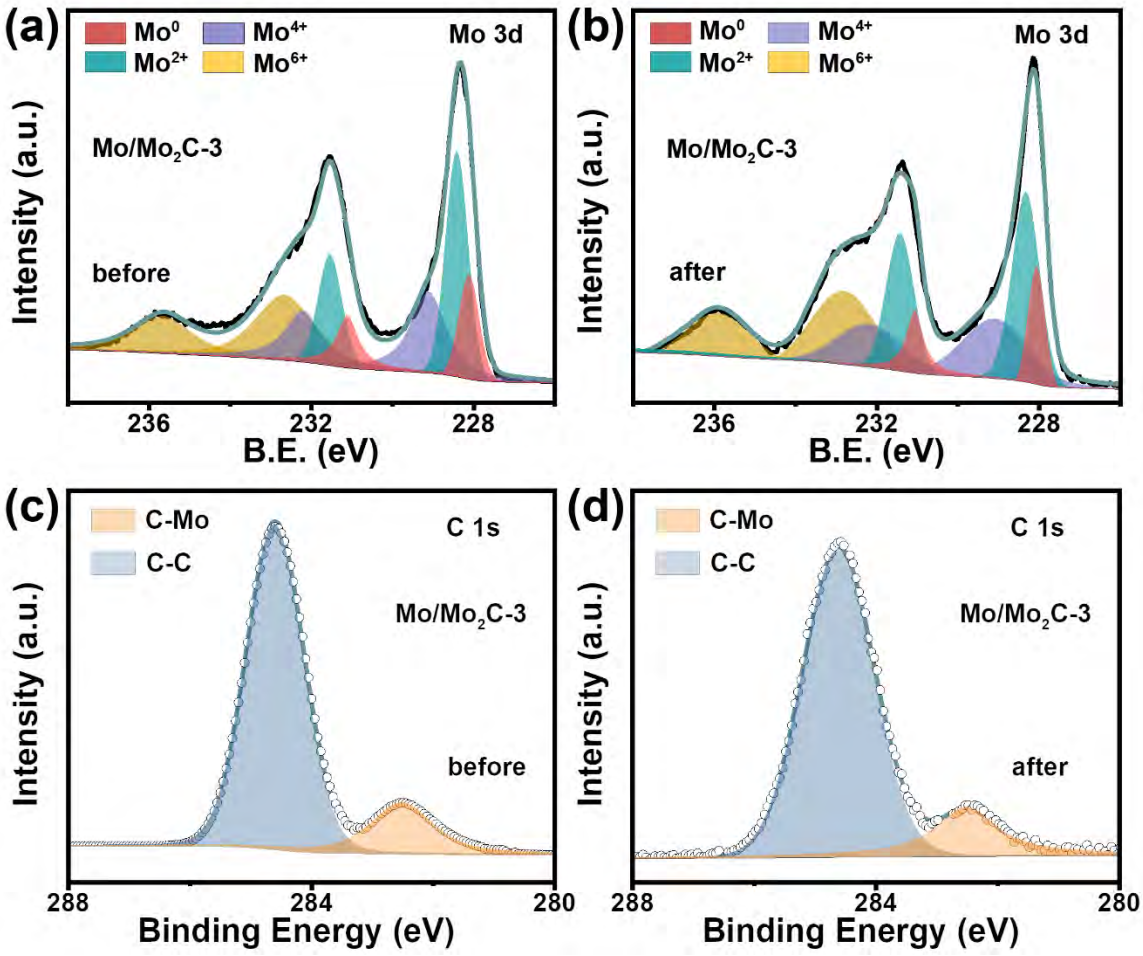

Figure S11. The high-resolution Mo 3*d* and C *1s* XPS spectra of Mo/Mo_2C-3: (a, c) Before and (b, d) After the HER stability test.

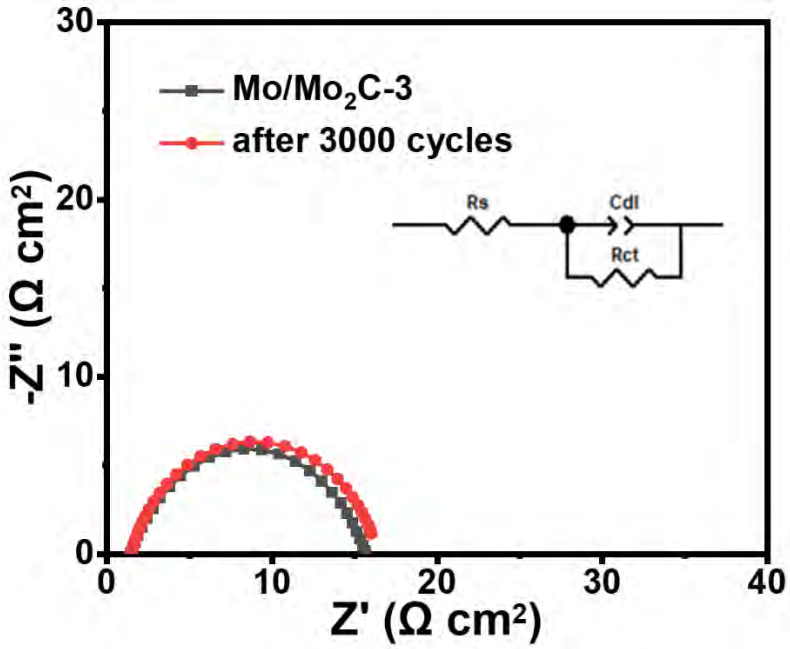

Figure S12. Nyquist plots of Mo/Mo_2C-3 before and after the HER durability test. (Error estimates through three times of independent tests).

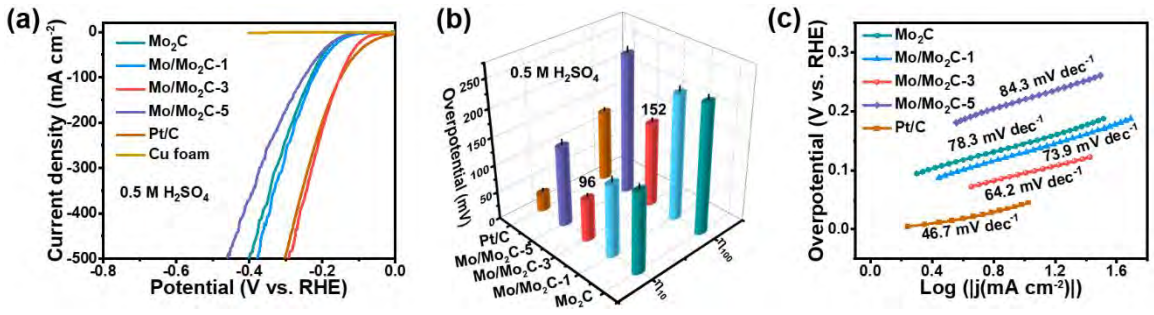

Figure S13. (a) LSV curves and (b) Overpotentials at 10 and 100 mA cm^{-2} of Mo_2C, Mo/Mo_2C-1, Mo/Mo_2C-3, Mo/Mo_2C-5, and Pt/C in 0.5 H_2SO_4; (c) Corresponding Tafel plots in 0.5 M H_2SO_4. (Error estimates through three times of independent tests).

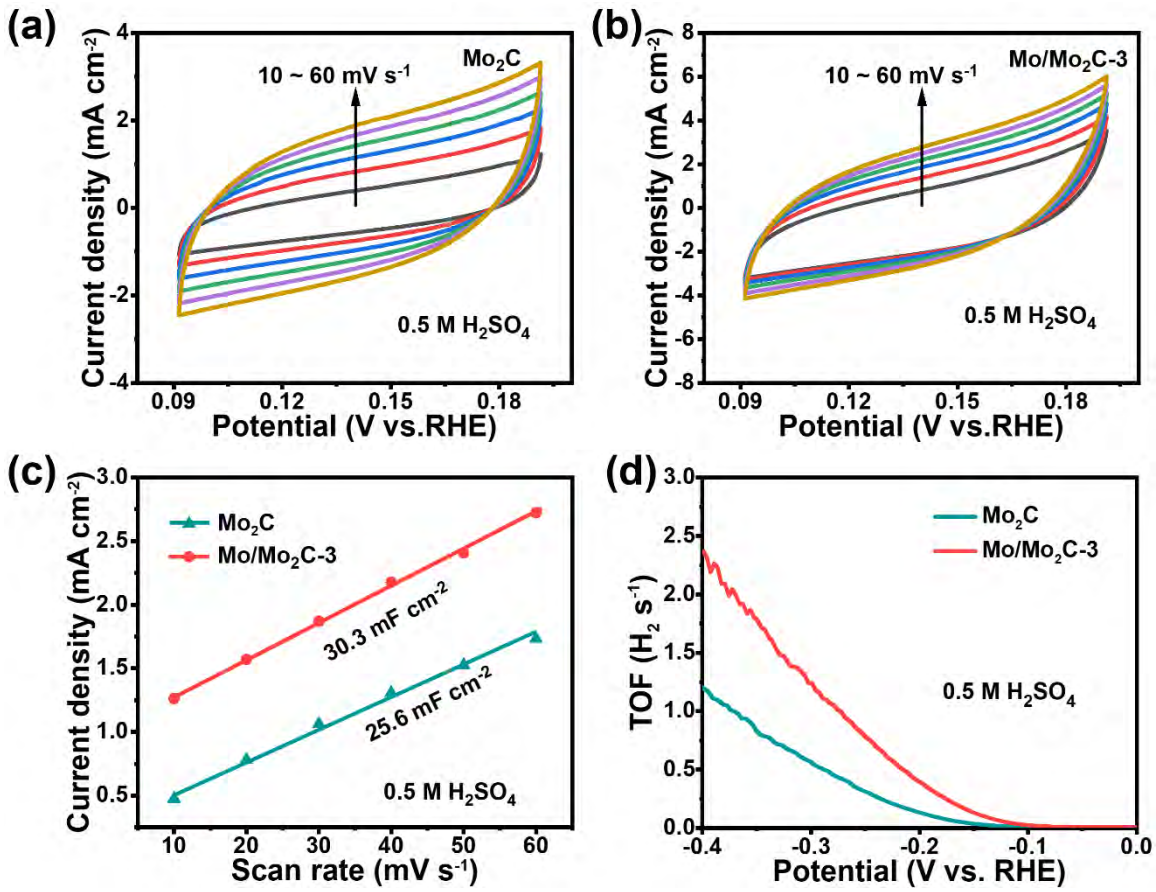

Figure S14. CV curves of (a) Mo_2C and (b) Mo/Mo_2C-3 at different scanning rates from 10 to 60 mV s^{-1} in 0.5 M H_2SO_4; (c) Corresponding double-layer capacitance (C_{dl}) and (d) TOF plots in 0.5 M H_2SO_4. (Error estimates through three times of independent tests).

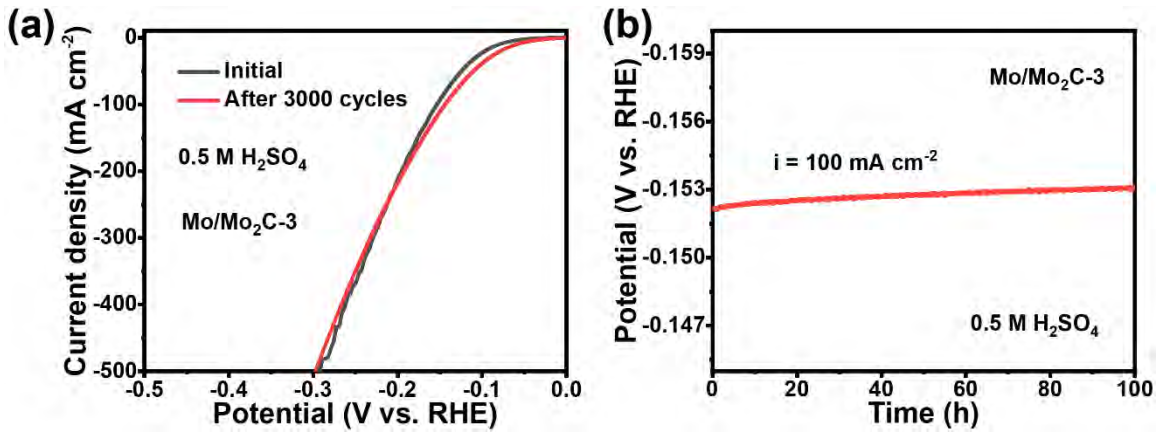

Figure S15. (a) Polarization curves of Mo/Mo_2C-3 before and after 3,000 CV cycles in 0.5 M H_2SO_4; (b) Stability test of Mo/Mo_2C-3 at 100 mA cm^{-2} in 0.5 M H_2SO_4 for 100 h. (Error estimates through three times of independent tests).

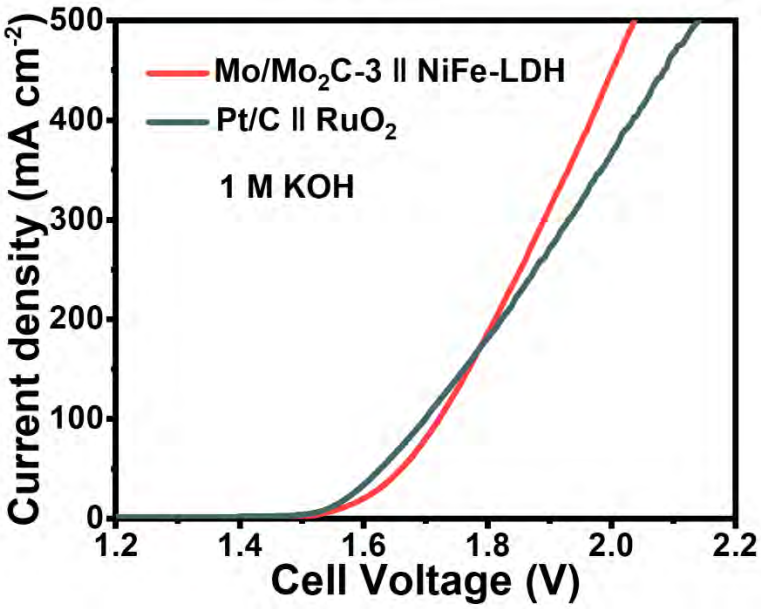

Figure S16. Polarization curves of the Mo/Mo_2C-3||NiFe-LDH and Pt/C||RuO_2 pairs in overall water splitting in 1 M KOH. (Error estimates through three times of independent tests).

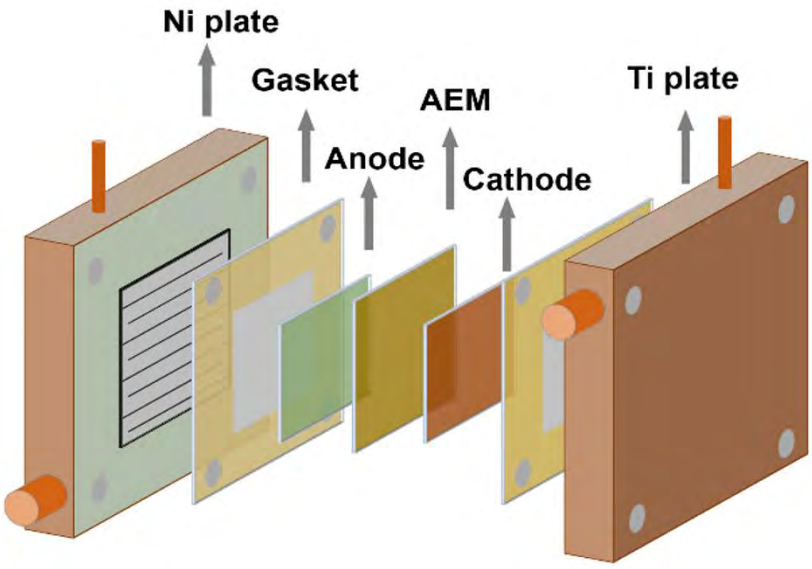

Figure S17. schematic illustration of the electrolyser structure.

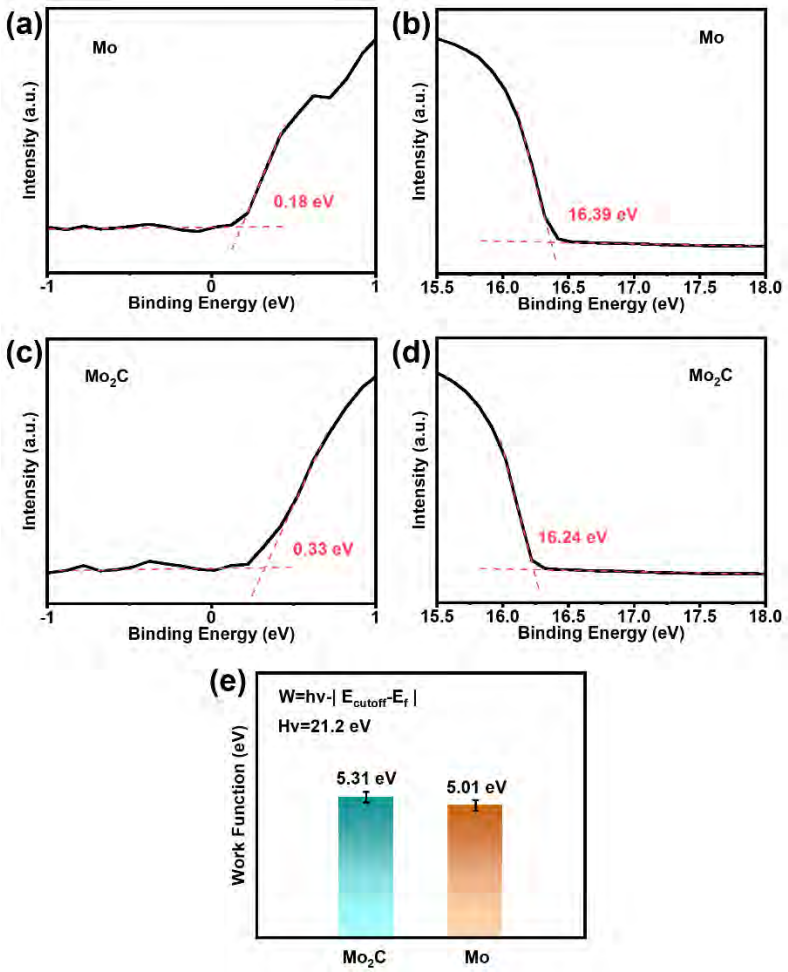

Figure S18. UPS results of (a-b) Mo powder and (c-d) Mo_2C after repeated fitting (n = 3); (e) Work functions of Mo and Mo_2C.

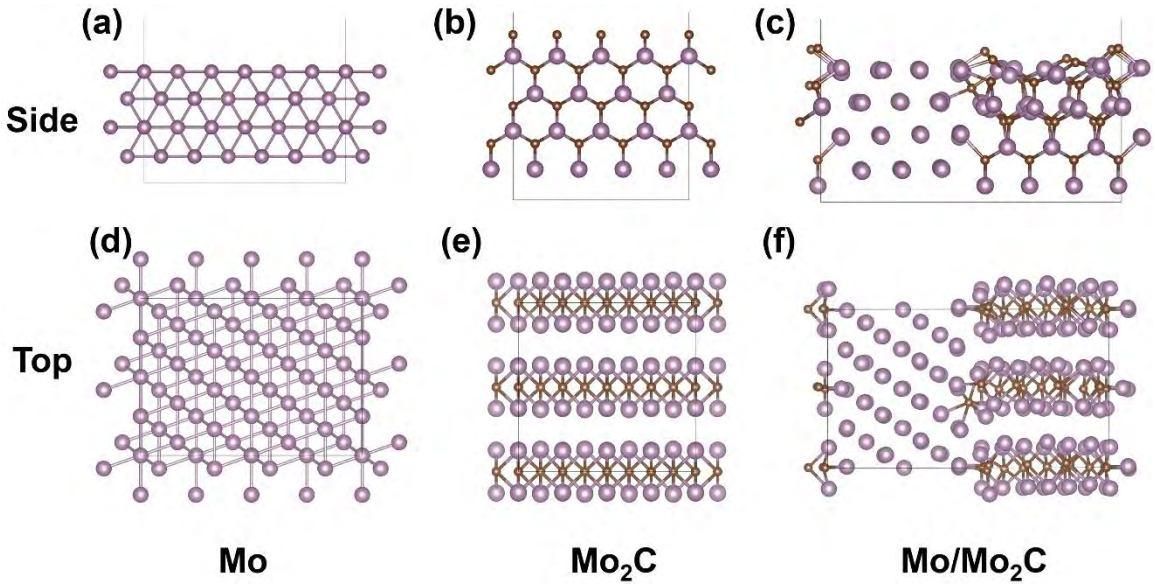

Figure S19. (a-c) Side-view atomic structure of Mo, Mo_2C, and Mo/Mo_2C; (d-f) Top-view atomic structure of Mo, Mo_2C, and Mo/Mo_2C.

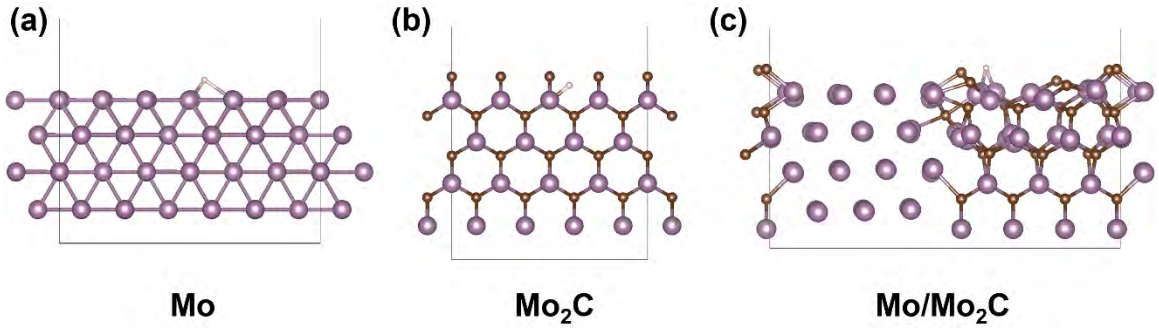

Figure S20. Side view of the schematic models of (a) Mo, (b) Mo_2C, and (c) Mo/Mo_2C with H_{ad} atoms.

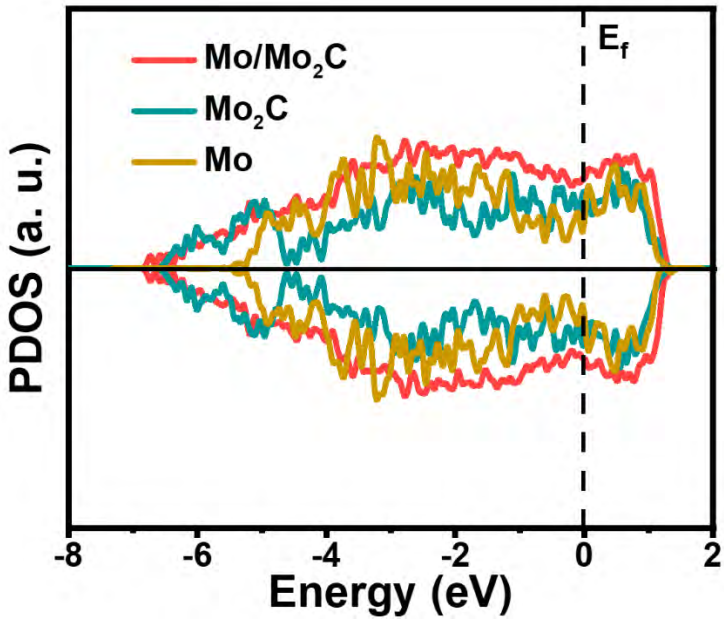

Figure S21. PDOS of Mo, Mo_2C, and Mo/Mo_2C.

Table S1. Comparison between Mo/Mo_2C and other recently reported catalysts in 1 M KOH. (Error estimates through three times of independent tests).

Electrocatalysts	Electrolytes	Overpotential of η_{10} (mV)	Tafel slope ($mV\ dec^{-1}$)	Refs.
MoC-Mo_2C	1 M KOH	98.2	59	[1]
Ni/Mo_2C-PC	1 M KOH	179	101	[2]
Zn-MoC/Mo_2C	1 M KOH	139	49.8	[3]
2D Mo_2C	1 M KOH	152	40.2	[4]
Mo_2C@NCS	1 M KOH	147	77	[5]
MoC/C-Ns	1 M KOH	92	51	[6]
Co-NC@Mo_2C	1 M KOH	173	65	[7]
Mo_2C/MoO_2	1 M KOH	204	87	[8]

v-Mo_xC	1 M KOH	116	60.4	[9]
MoC/MoP/BCNC	1 M KOH	137	65	[10]
Mo_2C/MoO_2	1 M KOH	127.3	67.5	[11]
β-Mo_2C/MoO_2	1 M KOH	99.8	60.16	[12]
Mo_2C/C	1 M KOH	132	88	[13]
Mo/Mo_2C	**1 M KOH**	**90**	**54.9**	**This work**

Table S2. Comparison between Mo/Mo_2C and other recently reported catalysts in 0.5 M H_2SO_4. (Error estimates through three times of independent tests).

Electrocatalysts	Electrolytes	Overpotential of η_{10} (mV)	Tafel slope (mV dec^{-1})	Refs.
MoC-Mo_2C	0.5 M H_2SO_4	114	62	[1]
Ni/Mo_2C-PC	0.5 M H_2SO_4	--	--	[2]
Zn-MoC/Mo_2C	0.5 M H_2SO_4	179	66.5	[3]
2D Mo_2C	0.5 M H_2SO_4	152	40.2	[4]
Mo_2C@NCS	0.5 M H_2SO_4	200	70.5	[5]
MoC/C-Ns	0.5 M H_2SO_4	126	69	[6]
Co-NC@Mo_2C	0.5 M H_2SO_4	143	60	[7]
Mo_2C/MoO_2	0.5 M H_2SO_4	168	58	[8]

v-Mo_xC	0.5 M H_2SO_4	130	69.6	[9]
MoC/MoP/BCNC	0.5 M H_2SO_4	158	58	[10]
Mo_2C/MoO_2	0.5 M H_2SO_4	119.5	78.5	[11]
Mo_2C/C	0.5 M H_2SO_4	185	84	[13]
Mo/Mo_2C	0.5 M H_2SO_4	**96**	**64.2**	**This work**

References

[1] W. Liu, X. Wang, F. Wang, K. Du, Z. Zhang, Y. Guo, H. Yin, D. Wang, A durable and pH-universal self-standing MoC-Mo_2C heterojunction electrode for efficient hydrogen evolution reaction, Nat. Commun. 12 (2021) 6776.

[2] Z. Yu, Y. Duan, M. Gao, C. Lang, Y. Zheng, S. Yu, A one-dimensional porous carbon-supported Ni-Mo_2C dual catalyst for efficient water splitting, Chem. Sci. 8 (2017) 968-973.

[3] C. Yang, R. Zhao, H. Xiang, J. Wu, W. Zhong, X. Li, Q. Zhang, Structural transformation of molybdenum carbide with extensive active centers for superior hydrogen evolution, Nano Energy 98 (2022) 107232.

[4] Y. Wang, W. Hong, C. Jian, X. He, Q. Caia, W. Liu, The intrinsic hydrogen evolution performance of 2D molybdenum carbide, J. Mater. Chem. A 8 (2020) 24204-24211.

[5] J. Ren, L. Chen, D. Yang, Z. Yuan, Molybdenum-based nanoparticles (Mo_2C, MoP and MoS_2) coupled heteroatoms-doped carbon nanosheets for efficient hydrogen evolution reaction, Appl. Catal. B: Environ. 263 (2020) 118352.

[6] B. Gao, Y. Huang, S. Wang, H. Lu, L. Zheng, X. Fan, X. Yang, W. Zhang, Y. Wang, Y. Zhang, Q. Gao, Y. Tang, MoC nanodots toward efficient electrocatalytic hydrogen evolution: an interlayer-confined strategy with a 2D-zeolite precursor, J. Mater. Chem. A 9 (2021) 4724-4733.

[7] Q. Liang, H. Jin, Z. Wang, Y. Xiong, S. Mu, Metal-organic frameworks derived reverse-encapsulation Co-NC@Mo_2C complex for efficient overall water splitting, Nano Energy 57 (2019) 746-752.

[8] M. Liu, Y. Yang, X. Luan, X. Dai, X. Zhang, J. Yong, H. Qiao, H. Zhao, W. Song, X. Huang, Interface-synergistically enhanced acidic, neutral and alkaline hydrogen evolution reaction over Mo_2C-MoO_2 heteronanorods, ACS Sustainable Chem. Eng. 6 (2018) 14356-14364.

[9] S. Kim, C. Choi, J. Hwang, J. Park, J. Jeong, H. Jun, S. Lee, S.-K. Kim, J.H. Jang, Y. Jung, J. Lee, Interaction mediator assisted synthesis of mesoporous molybdenum carbide Mo-valence state adjustment for optimizing hydrogen evolution, ACS Nano 14 (2020) 4988-4999.

[10] N. Chen, Q. Mo, L. He, X. Huang, L. Yang, J. Zeng, Q. Gao, Heterostructured MoC-MoP-N-doped carbon nanofibers as efficient, Electrochim. Acta 299 (2019) 708-716.

[11] A. Huang, H. Huang, F. Wang, N. Ke, C. Tan, L. Hao, X. Xu, Y. Xian, S. Agathopoulos, Mo_2C-based ceramic electrode with high stability and catalytic activity for hydrogen evolution reaction at high current density, Small 20 (2024) 2308068.

[12] W. Chen, M. Niu, Z. Zhang, L. Chen, X. Li, J. Zhang, R. Sun, H. Cao, X. Wang, Phase-Transition of Mo_2C induced by tungsten doping as heterointerface-rich electrocatalyst for optimizing hydrogen evolution activity, Small 20 (2024) 2311026.

[13] X. Chen, H. Liu, A. Jiang, X. Li, J. Xiao, Highly efficient electrocatalytic hydrogen evolution by double-shelled hollow spheres with Mo_2C/C heterostructure, Appl. Surf. Sci. (2025) 162869.